Horizontal distribution of tropospheric NO_2 and aerosols derived by dual-scan multi-wavelength MAX-DOAS measurements in Uccle, Belgium

Ermioni Dimitropoulou[1], François Hendrick[1], Martina M. Friedrich[1], Frederik Tack[1], Gaia Pinardi[1], Alexis Merlaud[1], Caroline Fayt[1], Christian Hermans[1], Frans Fierens[2] and Michel Van Roozendael[1]

[1] Royal Belgian Institute for Space Aeronomy (BIRA-IASB), Brussels, 1180, Belgium
[2] IRCEL-CELINE, Brussels, Belgium

Correspondence to: Ermioni Dimitropoulou (ermioni.dimitropoulou@aeronomie.be)

Abstract

Dual-scan ground-based Multi-AXis Differential Optical Absorption Spectroscopy (MAX-DOAS) measurements of tropospheric nitrogen dioxide (NO_2) and aerosols were carried out in Uccle (50.8°N, 4.35°E; Brussels region, Belgium) for two years, from March 2018 to February 2020. The MAX-DOAS instrument was operating in both UV and Visible wavelength ranges in a dual-scan configuration consisting of two sub-modes: (1) an elevation scan in a fixed viewing azimuthal direction and (2) an azimuthal scan in a fixed low elevation angle (2°). By analyzing the O_4 and NO_2 dSCDs at six different wavelength intervals along every azimuthal direction and by applying a new Optimal-Estimation-based inversion approach (the so-called mapping MAX-DOAS technique), the horizontal distribution of the NO_2 near-surface concentrations and vertical column densities (VCDs) and the aerosols near-surface extinction coefficient are retrieved along ten azimuthal directions. The retrieved horizontal NO_2 concentration profiles allow the identification of the main NO_2 hotspots in the Brussels area. Correlative comparisons of the retrieved horizontal NO_2 distribution were conducted with airborne, mobile, air-quality model, and satellite datasets, and overall a good agreement is found. The comparison with TROPOMI observations, from operational and scientific data products, reveals that the characterization of the horizontal distribution of tropospheric NO_2 VCDs by ground-based measurements, the appropriate sampling of TROPOMI pixels, and an adequate a priori NO_2 profile shape in TROPOMI retrievals lead to a better consistency between satellite and ground-based datasets.

1 Introduction

Aerosols and nitrogen dioxide (NO_2) play a crucial role in the tropospheric chemistry. NO_2 is an important tropospheric pollutant mainly emitted by combustion processes and nitrogen fertilizers used in agriculture (Seinfeld and Pandis, 1998). Traffic, domestic heating, industrial activities, and power plants are the largest NO_2 emitters (Tack et al., 2021). Beyond its harmful effects on human health (Chen et al., 2007), NO_2 participates in the formation of tropospheric ozone (O_3) by a non-linear photochemical mechanism which involves volatile organic compounds (VOCs).

30   Aerosols with a small diameter can penetrate deeply into the lungs, causing millions of premature deaths around the world per year (Khomenko et al., 2021). Additionally, aerosols influence the Earth's climate system by changing its radiation budget by scattering and absorbing sunlight (Quaas et al., 2008). In the boundary layer of urban regions, the horizontal distribution of NO_2 is highly heterogeneous given the fact that it is a short-lived species (Beirle et al., 2003). For those reasons, the regional and global monitoring of NO_2 and aerosols at high spatial resolution is crucial.

35   Since 1995, with the ERS-2 GOME (Global Ozone Monitoring Experiment) instrument (Burrows et al., 1999), satellite nadir air-quality measurements of atmospheric backscattered sunlight in the UV-visible range have provided daily global tropospheric column measurements of numerous trace gases, such as NO_2. Many satellite missions dedicated to air-quality monitoring followed over the next years with increasing spatial resolution. More recently, the TROPOspheric Monitoring Instrument (TROPOMI) sensor launched onboard the Sentinel-5P Precursor (S5P) platform in October 2017 reached an initial

40   spatial resolution of 7x3.5 km^2, and augmented on 6 August 2019 to 5.5x3.5 km^2. Due to TROPOMI's fine spatial resolution, monitoring the horizontal distribution of NO_2 in urban regions and identifying specific emission sources is made easier than with previous satellite missions but still, TROPOMI cannot fully capture the fine-scale (sub-kilometer) structures in the effective NO_2 field. Consequently, TROPOMI requires further attention concerning its measurements validation.

      Tropospheric vertical columns of many trace gases like NO_2, formaldehyde (HCHO), sulphur dioxide (SO_2), nitrous acid

45   (HONO) and O_3 can be retrieved by the Multi-AXis Differential Optical Absorption Spectroscopy (MAX-DOAS) technique (Hönninger et al., 2004; Wittrock et al., 2004; Pinardi et al., 2008, 2013; Clémer et al., 2010; Hendrick et al., 2014; Irie et al., 2011, 2012; Sinreich et al., 2007; Wagner et al., 2011; Wang et al., 2018). In recent years, MAX-DOAS measurements have been widely used as reference datasets for the validation of nadir airborne and space-borne air-quality measurements. MAX-DOAS instruments measure the scattered sunlight in the UV and Visible spectral ranges at multiple elevation angles above the

50   horizon. For absorbers located close to the surface, such as tropospheric NO_2, the higher sensitivity is achieved for low MAX-DOAS elevation angles. During the last years, MAX-DOAS measurements in more than one azimuthal direction are emerging (Ortega et al., 2016; Wang et al., 2014; Chan et al., 2020; Schreier et al., 2021). Multi-azimuthal MAX-DOAS measurements offer many possibilities on air-quality monitoring, such as a better characterization of the effective NO_2 field around the station. These ground-based datasets can be valuable for validating satellite missions with fine spatial resolution in regions where the

55   NO_2 horizontal distribution is heterogeneous, such as urban and sub-urban areas.

      In this study, a new aerosol and NO_2 horizontal distribution inversion approach based on two years (March 2018-February 2020) of dual-scan multi-wavelength MAX-DOAS measurements in Uccle (Brussels-Capital region, Belgium) is presented. We refer to this new approach as mapping MAX-DOAS technique. In every azimuthal viewing direction, parameterized NO_2 near-surface concentrations, NO_2 tropospheric columns and aerosol extinctions measured at six different wavelengths are used

60   as input in a new horizontal distribution inversion approach. On this basis, the near-surface aerosol extinction and NO_2 horizontal distributions are retrieved at a spatial resolution of about 3km in a range of about 20 km around the measurement site. These horizontal profiles are used to validate collocated TROPOMI tropospheric NO_2 columns. We use here (i) the operational TROPOMI data product, (ii) a so-called diagnostic data set, which is a small sample but with major updates

compared to the operational product (van Geffen et al., 2021b) and (ii) a European TROPOMI product where profiles from
65 CAMS regional CTM ensemble (S5P-CAMS) are used (Douros et al., 2021). One complete year of data (March 2018-March 2019) and two wavelength intervals (one in the UV and one in the Visible) have already been used in Dimitropoulou et al. (2020). It is proven that multi-azimuthal (the so-called dual-scan) MAX-DOAS measurements significantly improve the agreement between ground-based and TROPOMI tropospheric NO_2 column observations over the Brussels' area. By adding the multi-wavelength aspect, the present work represents an extension of the former study.

70 The manuscript is organized into six sections: in Sect. 2, the measurement site with the MAX-DOAS experimental set-up and the multi-wavelength DOAS analysis are presented. In Sect. 3, the TROPOMI tropospheric NO_2 measurements are described. Section 4 is composed of two main parts: Sect. 4.1 is a detailed description of the dual-scan multi-wavelength MAX-DOAS retrieval method and Sect. 4.2 is the horizontal aerosol and NO_2 distribution inversion approach (i.e., the mapping MAX-DOAS technique). In Sect. 5, main results followed by correlative comparisons of the retrieved ground-based and satellite
75 horizontal NO_2 distribution are presented. Finally, in Sect. 6, conclusions and future perspectives are given.

2 Dual-scan multi-wavelength MAX-DOAS measurements

2.1 Measurement site and experiment set-up

Brussels-Capital Region is the most densely populated area in Belgium, where pollutant concentrations, such as NO_2, are often high because of anthropogenic activities (Tack et al., 2021).

80 A MAX-DOAS dual-scan instrument was operated by BIRA-IASB (Koninklijk Belgisch Instituut voor Ruimte-Aeronomie – Institut Royal d'Aeronomie Spatiale de Belgique) in Uccle from January 2017 to February 2020. Uccle is located to the South of the city-center of Brussels and to the West of a large forested area (Bois de la Cambre). Therefore, it is an ideal site to perform MAX-DOAS observations under moderate to high pollution level conditions. Additionally, the characterization of the horizontal distribution of NO_2 and aerosols at high spatial resolution is of great interest here because of the heterogeneity of
85 the pollution sources (car traffic, national airport, power plant) in the capital region of Brussels.

The MAX-DOAS dual-scan instrument is composed of the following parts: the optical head mounted on a sun tracker, two spectrometers (UV and Visible) inside a thermo-regulated box and the data-acquisition unit. The optical head and the two spectrometers are connected with optical fibers. A more detailed description of the BIRA-IASB MAX-DOAS dual-scan instrument can be found in Dimitropoulou et al. (2020).

90 From March 2018 to February 2020, the MAX-DOAS instrument operated in a dual-scan viewing mode. Two different sub-modes compose one complete measurement scan (see Dimitropoulou et al., 2020): (1) a vertical scan in nine different elevation angles (EAs) in one fixed telescope azimuth angle (TAA; Northeast direction i.e., towards the city center and the national airport) and (2) a horizontal scan in nine different azimuthal directions at a fixed elevation angle (2° above the horizon).

Several azimuthal viewing directions were tested to obtain an optimal horizontal sampling without any obstacle in the different
95 viewing directions (see Fig. 1). The selection of more azimuthal directions towards the North, Northeast, and Northwest was

made considering the location of the main NO₂ emission sources and, consequently, the highly variable NO₂ horizontal distribution towards these directions.

The integration time for each measured radiance spectrum is 60s, resulting in a full scan duration of approximately 20 minutes.

100
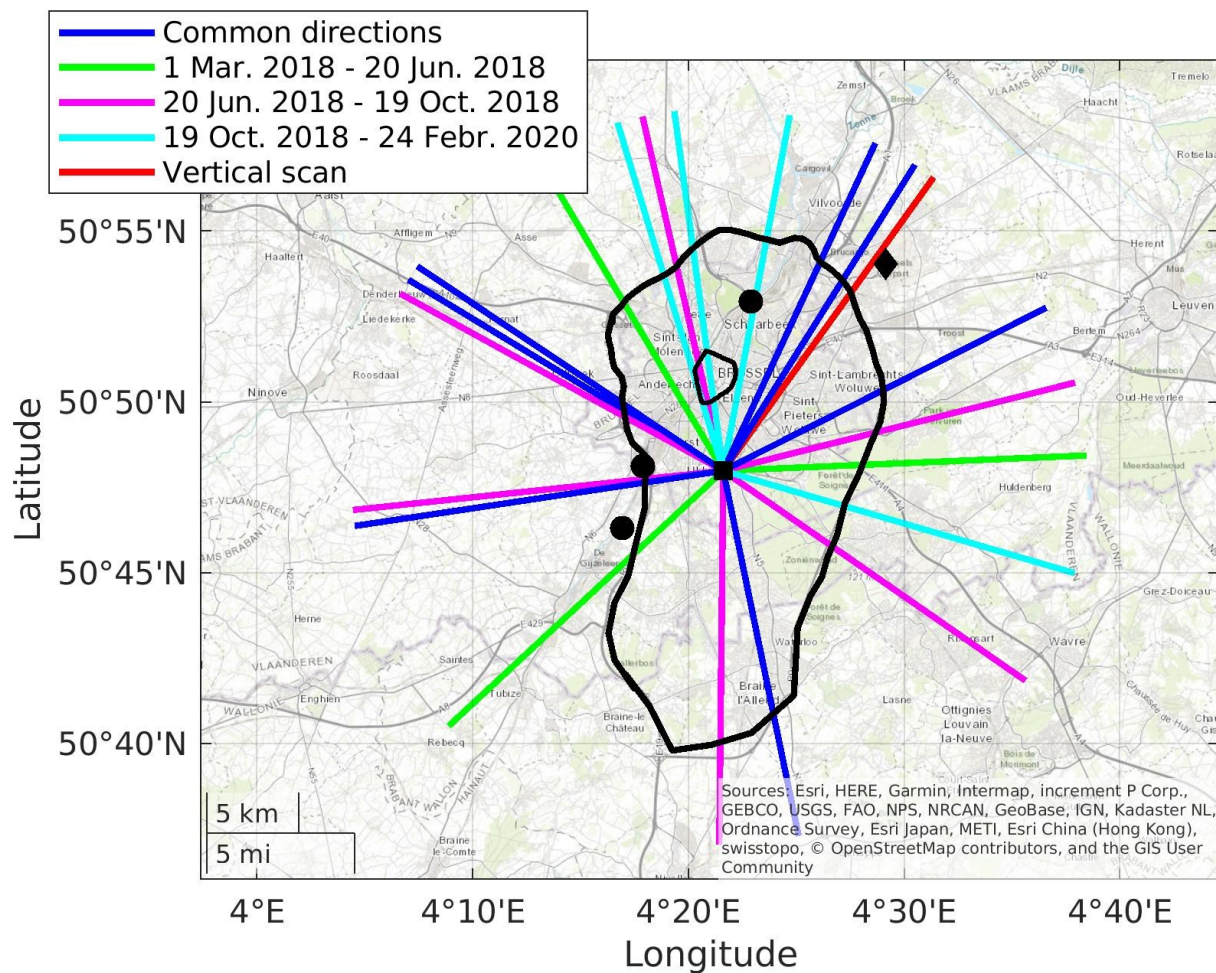
Figure 1. The experimental set-up of the BIRA-IASB dual-scan MAX-DOAS instrument. Each line is color-coded
105 **according to the different set-ups that were used from March 2018 to February 2020. The length of each line is equal**
to 20 km, which corresponds to the typical horizontal sensitivity for the MAX-DOAS measurements in the present
study (see Fig. 18). The black square shows the MAX-DOAS instrument location, the black polygon the National

Airport, the black dots the NO$_2$ hotspots emitting more than 10 kg of NO$_x$ per hour (Emission Inventory of the Belgian Interregional Environment Agency, 2017) , and the black line represents the Brussels Ring motorway.

110

2.2 Multi-wavelength DOAS analysis

The measured radiance spectra of a full measurement scan are analyzed using the QDOAS spectral fitting software developed by BIRA-IASB (Fayt et al., 2011). The DOAS technique separates the narrow absorption features of trace gases in the UV-Visible spectral range from a spectral background caused mainly by Mie and Rayleigh scattering and instrumental effects. The

115 trace gas concentration integrated along the light-path in a measured spectrum relative to the amount of the same absorber in a reference spectrum is the primary product of the DOAS analysis and is called differential slant column density (dSCD). Here, average zenith spectra before and after each measurement scan are used as a reference.

The O$_4$ and NO$_2$ dSCDs are retrieved in six different wavelength intervals: Three intervals in the UV spectral range (330-361 nm, 350-370 nm, and 360-383.5 nm) and three in the Visible range (420-460 nm, 450-490 nm, and 510-540.1 nm). These

120 fitting windows were selected to optimize the determination of the O$_4$ and NO$_2$ dSCDs at the maximum number of different O$_4$ absorption bands available in the wavelength domain of the instrument. Figure 2 shows an example of the O$_4$ and NO$_2$ fits in all the intervals used in the present work. In each chosen fitting window, we select a reference wavelength, which corresponds to the maximum of an O$_4$ absorption peak (or close to it) in the respective wavelength intervals (see Fig. 2), and it is subsequently used for radiative transport calculations and further analysis. The different reference wavelengths are 343

125 nm, 360 nm, 380 nm, 447 nm, 477 nm and 530 nm (see Fig. 2). To optimize the derivation of the dSCDs at the six selected wavelengths, the fit of a slope parameter, which accounts for the variation of the dSCD within the fitting interval (Puķīte et al., 2010), is necessary. This is especially important when the reference wavelength is not located in the center of the fitting window (i.e., 330-361 nm, 350-370 nm, 420-460 nm, and 450-490 nm). The DOAS settings used for each fitting interval are presented in Table S1. As shown in this table, two different O$_4$ cross-sections are used in this study: (1) Finkenzeller (private

130 communication) in the UV fitting intervals and (2) Thalman and Volkamer, (2013) in the Vis fitting intervals. The main motivation for using the O$_4$ cross-section from Finkenzeller (measured at 25°C) in the UV fitting intervals is the significant improvement of the fit quality and the reduction of the uncertainties for the UV retrievals. Sensitivity tests and comparisons with radiative transport simulations also show that the resulting O$_4$ and NO$_2$ dSCDs are consistent throughout the whole wavelength range covered by the six intervals. For NO$_2$ and O$_3$, which are the strongest absorbers in all the fitting windows,

135 a correction for the solar I$_0$ effect (Aliwell et al., 2002) is applied. A high-resolution solar atlas (Kurucz et al., 1984) is used for the wavelength calibration of the measured spectra.

140
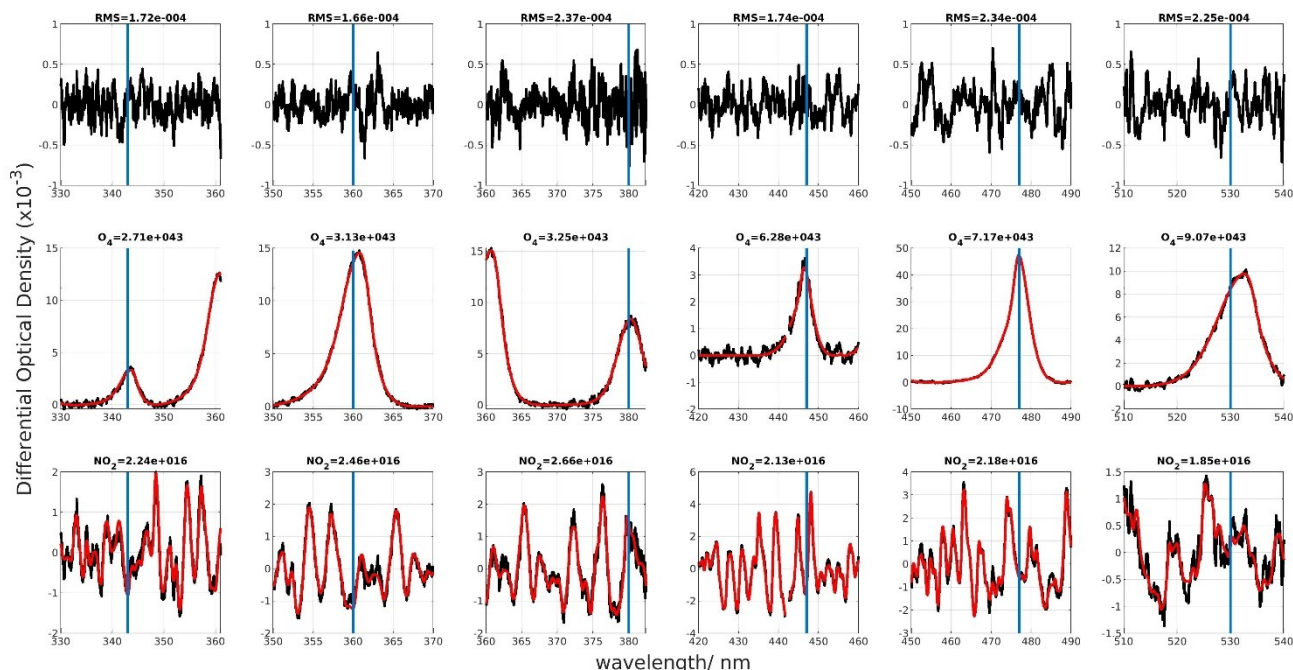
Figure 2. Fit results of the O₄ and NO₂ fit at the six selected fitting windows from the dual-scan MAX-DOAS measurements in Uccle (2 June 2019 at 07:05 UTC). The measured spectra are represented with black lines, while the fit results are shown with red lines. The blue lines represent the six reference wavelengths.

3 TROPOMI tropospheric NO₂ measurements

In the present study, MAX-DOAS tropospheric NO_2 VCDs are used to validate collocated TROPOMI satellite observations. TROPOMI is a passive grating imaging spectrometer flying onboard the S5P satellite platform. It covers the UV-Visible (250-500 nm), near-infrared (710-770 nm), and short-wave infrared (2314-2382 nm) spectral ranges (Veefkind et al., 2011). TROPOMI measures in a push-broom configuration with a full swath width as wide as 2600 km, and it provides daily global coverage at a spatial resolution (true-nadir pixel size) of 7x3.5 km², further improved to 5.5x3.5 km² on 6 August 2019. The TROPOMI tropospheric NO_2 algorithm has been developed at KNMI and uses a retrieval-assimilation-modeling system that is based on the 3-D global TM5 chemistry transport model (van Geffen et al., 2021a; Williams et al., 2017).

We use the reprocessed (RPRO) and offline (OFFL) datasets of the TROPOMI L2 tropospheric NO_2 column product (see Table 1 for the corresponding versions). According to the guidelines provided by van Geffen et al. (2021a), RPRO dataset are available only for the first period of the present study (see Table 1). For the remaining periods, OFFL datasets are used, which are the main data products being available within two weeks from the TROPOMI measurement. To ensure best measurements' quality, only pixels with a quality assurance value larger than 0.75 are used. This quality flagging eliminates pixels with a cloud radiance fraction larger than 0.5, snow or ice, and erroneous retrievals (Eskes and Eichmann, 2020).

Next to operational products, two additional TROPOMI data sets are also used (see Section S2 in the supplement). In the first one, the TROPOMI retrieval is performed with different a priori profiles (Douros et al., in preparation). The coarse TM5-MP a priori NO_2 profiles, using a spatial resolution of 1° x 1°, is replaced by NO_2 profile shapes from the CAMS (Copernicus Atmospheric Monitoring Service) regional Chemistry Transport Model (CTM) ensemble at a spatial resolution of 0.1° x 0.1° (S5P-CAMS product). The replacement of a coarse a priori information by a finer one can lead to significant changes in the TROPOMI retrieved NO_2 tropospheric columns. The available dataset covers October 2018 to March 2020 (OFFL dataset, L2, and version 01.02.00 up to 01.04.00, Eskes and Eichmann, 2020).

In the second additional product, the TROPOMI retrieval is performed with an improved cloud product (Eskes et al., 2020; van Geffen et al., 2021a). According to van Geffen et al. (2021a), the improvement in the FRESCO-S cloud pressure retrieval scheme to the FRESCO-wide product, has an impact on the NO_2 AMFs and consequently, on the NO_2 tropospheric columns over polluted areas. More precisely, the existing FRESCO-S product had a negative bias in the cloud height values, which resulted in a low NO_2 tropospheric column (Compernolle et al., 2021). The TROPOMI tropospheric NO_2 columns are retrieved using an improved FRESCO-S cloud retrieval scheme, called FRESCO-wide, in v1.4 since 29 November 2020 (Eskes and Eichmann, 2020). In the present study, the diagnostic data sets (DDSv2) are used, which are an ensemble of reprocessed data for past periods analyzed with new versions (van Geffen et al., 2021b). Over the MAX-DOAS measurement time-period, only DDSv2 data corresponding to OFFL datasets (v1.2 and v1.3) are available. Excluding the spin-up period needed by TM5-MP, only four data periods are available for our comparisons (i.e., 30/06/2018 - 06/07/2018, 30/12/2018 - 5/01/2019, 30/03/2019-05/04/2019, and 17/09/2019-23/09/2019).

Table 1. TROPOMI NO_2 processor versions used in the present study.

Dataset	Version	Starting date	End date
RPRO	01.02.02	30/04/2018	17/10/2018
OFFL	01.02.00	17/10/2018	28/11/2018
OFFL	01.02.02	28/11/2018	20/03/2019
OFFL	01.03.00	20/03/2019	23/04/2019
OFFL	01.03.01	23/04/2019	26/06/2019
OFFL	01.03.02	26/06/2019	29/11/2020

4 Description of the mapping MAX-DOAS technique

First, the measured radiance spectra in the UV and Visible wavelength ranges are analyzed in six different fitting windows with the main output being the O_4 and NO_2 dSCDs at six wavelengths, which are 343 nm, 360 nm, 380 nm, 447 nm, 477 nm

and 530 nm (see Section 2.2). Then, the OEM-based MMF algorithm is applied to the O_4 and NO_2 dSCDs in the main azimuthal direction (and at 477 nm) to retrieve vertical NO_2 profiles and obtain information about the vertical extent of NO_2 in the troposphere (MLH_{NO2}; see Section 4.1).

As an intermediate step, radiative transfer model (RTM) simulations are performed (see Table 2 and Section 4.2) to obtain information about the horizontal sensitivity (L_{NO2}) and AOD as a function of O_4 dSCDs, wavelength, and MLH_{NO2}.

Then, in the next step, a new dual-scan parameterization technique is applied to the O_4 and NO_2 dSCDs at the six different wavelengths and in all the azimuthal directions with MLH_{NO2}, measured O_4 dSCDs, and measurement geometry being the main input parameters to retrieve the horizontal sensitivity of NO_2 and, consequently, the NO_2 near-surface concentrations and VCDs, and near-surface aerosol extinction (see Section 4.2).

In the final step, a new OEM-based horizontal distribution inversion approach is developed using the six near-surface NO_2 concentrations and aerosol extinction values per azimuthal direction to retrieve horizontal NO_2 and aerosol extinction horizontal profiles in an output horizontal grid of 500m thickness (see Section 4.3).

A flow chart describing the mapping MAX-DOAS technique is shown in Fig. 3.
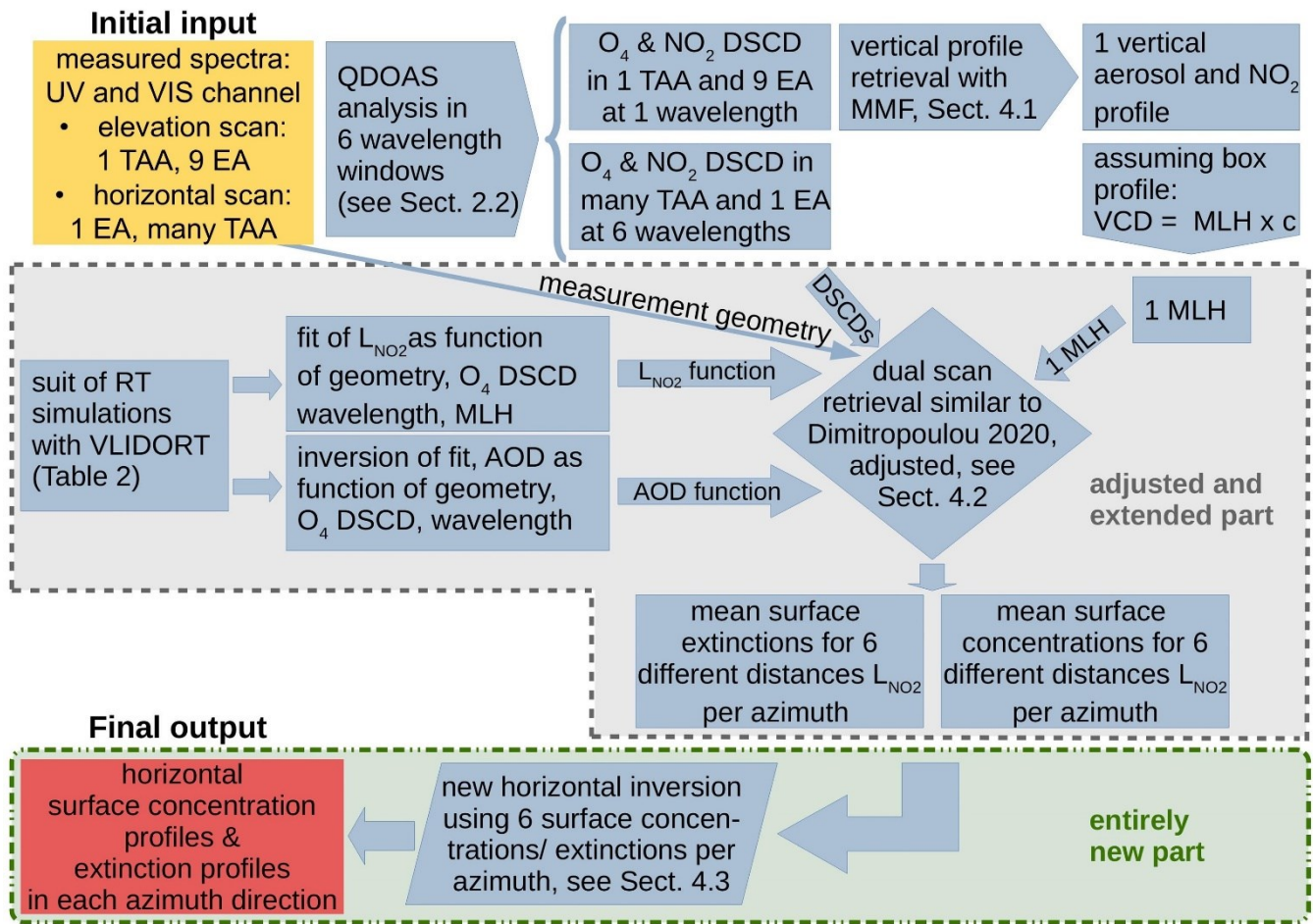
Figure 3. Mapping MAX-DOAS technique flow chart.

200

4.1 Aerosol and NO₂ OEM-based profile retrievals

The Optimal-estimation-based Mexican MAX-DOAS Fit (MMF) inversion algorithm (Friedrich et al., 2019) is applied to retrieve the aerosol extinction coefficient and NO_2 vertical profiles for each MAX-DOAS elevation scan in the main azimuthal direction at 360 nm and 477 nm. First, the O_4 measurements are used to retrieve the aerosol extinction profile. Several studies indicated the importance of applying a scaling factor ($\neq 1$) to the observed O_4 dSCDs to bring them in agreement with simulated O_4 dSCDs by radiative transfer modeling (Wagner et al., 2009; Clémer et al., 2010; Merlaud et al., 2011; see also Wagner et al., 2019 / Table 1 for a comprehensive list of all those studies). However, there is no consensus on the fundamental reason for applying this scaling (see e.g. Ortega et al., 2016). As found by Tirpitz et al. (2021), the choice of the scaling factor has only a small effect on the performance of the trace gas retrieval, so we decided not to apply it in the present study. The aerosol extinction profile retrieved from each scan is used as an input to the radiative transfer calculations used to retrieve the NO_2

retrieval profile. Further details about the MMF inversion algorithm, the input a priori parameters, the quality check of each scan, and the estimated uncertainties of the aerosol and NO$_2$ vertical profile can be found in Dimitropoulou et al. (2020).

A broken cloud-filtering approach based on Gielen et al. (2014) is applied to the MAX-DOAS measurements to exclude MAX-

215 DOAS aerosol and NO$_2$ scans influenced by the presence of clouds, which are known to potentially degrade the quality of the retrievals (Gielen et al. 2014, Wagner et al. 2014). Three sky conditions can be distinguished with this flagging approach: (1) clear sky, (2) homogeneous cloud coverage and (3) broken clouds conditions. Retrievals under broken cloud conditions are rejected from the present study.

The profile retrieval was performed to estimate the Mixing Layer Height of NO$_2$ (MLH$_{NO2}$). The MLH$_{NO2}$ is estimated per

220 measurement scan, and it is the ratio of VCD$_{NO2,main}$ to the NO$_2$ near-surface concentration (c$_{NO2,main}$) as retrieved in the main azimuthal direction by the MMF inversion algorithm:

$$\text{MLH}_{\text{NO}_2} = \frac{\text{VCD}_{NO2,main}}{c_{NO2,main}} \tag{1}$$

Therefore, during one measurement scan, two assumptions were made: (1) the homogeneous distribution of NO$_2$ inside the MLH$_{NO2}$ and (2) the homogeneous MLH$_{NO2}$ around the measurement site and its use in all the azimuthal directions. The validity

225 of the second assumption is tested in Section 4.2.3.

4.2 Dual-scan MAX-DOAS retrieval method

A complete MAX-DOAS measurement scan is composed of two different sub-scans, as described in Sect. 2.1. The aerosol and NO$_2$ vertical profiles are retrieved from the elevation scan in the main azimuthal direction. In the other azimuthal

230 directions, measurements are performed only in a single low elevation angle (2°), and therefore, the retrieval of aerosol and NO$_2$ vertical profiles is not possible. Using the fact that the lowest elevation angles have the highest sensitivity to trace gases located nearby the surface due to the long light path in this layer, a new dual-scan MAX-DOAS retrieval strategy was developed here. This new retrieval strategy is an extension of the work presented in Dimitropoulou et al. (2020) and aims to retrieve the near-surface NO$_2$ box-averaged volume mixing ratios (VMRs) and the NO$_2$ VCDs at six different wavelengths. In

235 Dimitropoulou et al. (2020), the applied dual-scan NO$_2$ MAX-DOAS retrieval was itself an adaptation of the parameterization technique proposed by Sinreich et al. (2013). More precisely, in the presence of sufficient aerosols in the atmosphere (i.e., sufficient aerosols to constrain the light path in a near-surface layer and ensure that the near-surface NO$_2$ concentration can be approximated by a near-surface box profile), the measured NO$_2$ dSCDs at one low elevation angle (2°) can be related to the near-surface NO$_2$ box-averaged concentration as follows:

240

$$\text{dSCD}_{\text{NO}_2} = c_{\text{NO}_2} L_{\text{NO}_2} \tag{2}$$

where dSCD$_{NO2}$ is the differential slant column density of NO$_2$ and c$_{NO2}$ its mean concentration along the differential effective light path, L$_{NO2}$.

245 Consequently, the knowledge of the differential effective light-path's length (i.e., L$_{NO2}$) is crucial to derive the near-surface NO$_2$ concentrations. The oxygen collisional complex (O$_4$) can be used as a tracer for the effective light-path in the atmosphere, as its concentration is well-known (it is the square of O$_2$ concentration). As a result, observed changes of the O$_4$ dSCDs can be directly attributed to changes in the light-path due to the presence of particles like aerosols and clouds. L$_{O4}$ is calculated as follows:

250

$$L_{O_4} = \frac{dSCD_{O_4}}{c_{O_4}} \tag{3}$$

where c$_{O4}$ is the typical O$_4$ concentration at the altitude of the instrument.

However, the direct use of the O$_4$ light-path length in the NO$_2$ retrieval is not possible under moderate to high pollution
255 conditions, such as those in Brussels, because the profile shapes of O$_4$ and NO$_2$ are not the same. In Dimitropoulou et al. (2020), we used radiative transfer model (RTM) simulations to estimate a unitless correction factor, which accounts for these profile shape differences. This unitless correction factor indicates that under moderate to high pollution conditions, L$_{NO2}$ is equal to or smaller than L$_{O4}$. For a correction factor equal or close to one, L$_{O4}$ is equal to L$_{NO2,}$ which means that there is a moderate to high aerosol load in the atmosphere during the measurement. On the other hand, correction factors smaller than unity are
260 obtained for measurements performed under aerosol-free conditions or a thin MLH. Assuming a homogeneous NO$_2$ distribution inside the MLH, the MLH is derived from the NO$_2$ vertical profiles in the main azimuthal direction and is defined as the ratio of the NO$_2$ VCD to the near-surface concentration of NO$_2$. In Dimitropoulou et al. (2020), the RTM simulations were performed for eight different MLH values of aerosols and NO$_2$ in the range of 500-2000 m (i.e. eight different combinations) and for different measurement viewing geometries (Solar Zenith Angle (SZA), Relative Azimuth Angle (RAA)
265 and the corresponding elevation angle of 2°). For every MAX-DOAS measurement, one value of the correction factor is given according to its viewing geometry and MLH value during the measurement. For further information, we refer the reader to Dimitropoulou et al. (2020).

In the present study, a new dual-scan NO$_2$ MAX-DOAS retrieval method, which is more suitable for interpreting multi-wavelength measurements than the previous approach (Dimitropoulou et al., 2020), is developed. It is presented in detail in
270 the following subsection.

4.2.1 Developed dual-scan MAX-DOAS retrieval method

The main advantages of the new dual-scan NO$_2$ MAX-DOAS retrieval method (which are also the main differences with respect to Dimitropoulou et al., 2020) are the following: (1) the direct use of the measured O$_4$ dSCDs to estimate L$_{NO2}$ for every measurement, (2) retrieval of near-surface aerosol extinction close to the ground, and (3) the exploitation of the

275   wavelength dependency of the horizontal path representative of MAX-DOAS measurements for the retrieval of the horizontal distribution of aerosols (and therefore NO_2) around the measurement site. The latter is done using O_4 and NO_2 dSCDs measured at six different wavelengths. This new method is described below.

    Assuming that the NO_2 vertical distribution can be approximated by a box profile of height equal to mixing layer height (MLH_{NO2}), the following equation can be used:

280

$$c_{NO_2} = \frac{VCD_{NO_2}}{MLH_{NO_2}} = \frac{dSCD_{NO_2}}{L_{NO_2}} \tag{4}$$

This means that the NO_2 near-surface concentration can be expressed as a ratio of the $dSCD_{NO2}$ to the L_{NO2} (see Eq. 2) or as a ratio of the VCD_{NO2} to the MLH_{NO2}. When knowing MLH_{NO2} and VCD_{NO2}, L_{NO_2} can be simulated as follows:

285

$$L_{NO_2 \, simulated} = dSCD_{NO_2 \, simulated} \cdot \frac{MLH_{NO_2}}{VCD_{NO_2}} \tag{5}$$

    Here, NO_2 dSCDs and consequently L_{NO2} are simulated using the radiative transfer model VLIDORT version 2.7 (Spurr, 2006). Seasonal median MAX-DOAS NO_2 vertical profiles, as retrieved by applying the MMF inversion algorithm in the main
290   azimuthal direction (see Sect. 4.1), show that the bulk (70 %) of the NO_2 concentration is located inside the MLH_{NO2}, which is expected since MLH_{NO2} is estimated as the ratio of VCD_{NO2} to the near-surface NO_2 concentration. On the other hand, this is not the case for aerosols (only 30 % of the aerosol content is seen to be located inside the MLH_{NO2}). Considering this feature, for the VLIDORT simulations, the NO_2 a priori profiles are modeled as box profiles with a constant concentration equal to 1.5×10^{11} molec/cm^3 from the surface to the MLH_{NO2}. Two layers compose the aerosol a priori profiles: (1) the MLH_{NO2} and
295   (2) the free troposphere. The equation, which is applied to estimate the aerosol extinction profile a(z), is the following (see Wang et al., 2014):

$$a(z) = AOD \frac{p}{MLH_{NO_2}}, \text{ for } z \leq MLH_{NO_2} \tag{6a}$$

and,

$$a(z) = b(\xi, MLH_{NO2}, p) \exp(-\frac{z}{\xi}), \text{ for } z > MLH_{NO_2} \tag{6b}$$

300   where AOD is the aerosol optical depth, p is the fraction of AOD inside the MLH_{NO2}, b is a normalizing constant for the exponential component (Wang et al., 2014), z is the simulation altitude grid, and ξ is the scaling height for the aerosols located outside the MLH_{NO2}, which is set to 5 km (Wang et al., 2014). In the present study, the fraction of AOD located within the MLH_{NO2} is set to p=0.3 (see above). The effect of the p value and the NO_2 profile shape on the retrieved NO_2 near-surface VMRs and VCDs were investigated and considered in the error budget (see Sect. 4.2.2).
305   The MLH_{NO2} is a known parameter and it is estimated per measurement scan, as the ratio of VCD_{NO2} to the NO_2 near-surface concentration as retrieved in the main azimuthal direction by the MMF inversion algorithm.

The RTM simulations have in total nine input parameters, which are the elevation angle, SZA, RAA, AOD, MLH_{NO2}, c_{NO2}, AOD (p and ξ), and wavelength. It should be noted that the elevation angle is kept constant (i.e., 2º). For the six different wavelengths (343 nm, 360 nm, 380 nm, 447 nm, 477 nm, and 530 nm), we separately perform RTM simulations and L_{NO2} (see Eq. 5) are simulated for the assumed SZA, RAA, MLH_{NO2}, c_{NO2}, and AOD input scenarios presented in Table 2.

Table 2. RTM inputs for the simulations of L_{NO2} at the six selected wavelengths (343 nm, 360 nm, 380 nm, 447 nm, 477 nm, and 530 nm).

Parameter	Values
Wavelength/ nm	343, 360, 380, 447, 477, 530
SZA/ º	20, 30, 40, 50, 60, 70, 80
RAA/ º	0, 10, 20, 30, 40, 50, 60, 90, 120, 150, 180
AOD	0, 0.1, 0.3, 0.4, 0.6, 0.8, 1
p of AOD	0.30
ξ of AOD/ km	5
asymmetry parameter	0.68
Single Scattering Albedo (SSA)	0.92
MLH/ m	500, 1000, 1500
Elevation angle/ º	2
C_{NO2}/ molec.cm^{-3}	1.5×10^{11}

The simulated O_4 dSCDs are a function of the input parameter AOD. The relation between the simulated O_4 dSCDs and the input AOD values is shown in Fig. 4a. A Piecewise cubic hermite interpolating polynomial fitting through the AOD as a function of the simulated O_4 dSCDs for each SZA, RAA, and MLH_{NO2} combination can be used in order to perform an inverse method (i.e. to estimate the near-surface aerosol extinction from the measured O_4 dSCDs). Additionally, in Fig.4b, we can see that the relation between the O_4 dSCDs and the AOD values is valid for MAX-DOAS measurements.

For every combination of all eight parameters (i.e., all the parameters of Table 2, except the AOD values), a polynomial fit of simulated L_{NO2} as a function of simulated O_4 dSCDs is applied. Fig. 5a shows simulated L_{NO2} as a function of simulated O_4 dSCDs, and a second-order polynomial is fitted through the data points. We observe, also, in Fig. 5b, in which an example day of MAX-DOAS measurements is presented, that the L_{NO2} as a function of the measured O_4 dSCDs have the same relation as the simulated quantities. Since NO_2 is an optically thin absorber, L_{NO2} is not a function of c_{NO2} and consequently, a L_{NO2} value can be estimated by using the measured O_4 dSCD for each measurement. Based on the corresponding SZA, RAA, measured

O_4 dSCD, and MLH_{NO2}, a L_{NO2} is attributed to each low elevation MAX-DOAS measurement through this polynomial fit. To express L_{NO2} as a function of four different parameters (i.e., O_4 dSCD, SZA, RAA, and MLH_{NO2}), L_{NO2} is interpolated linearly at the O_4 dSCD, SZA, RAA, and MLH_{NO2} of each measurement. For example, a MAX-DOAS measurement with SZA=30°, RAA=60°, MLH_{NO2}=1km, and measured O_4 dSCD=6.10^{43} $molec^2.cm^{-5}$ will have a L_{NO2} equal to 15 km at 477 nm (see Fig. 5a).

Based on this approach, the near-surface NO_2 concentration can be calculated at the six different wavelengths by using the measured $dSCD_{NO2}$ together with the simulated L_{NO2} value (Eq. 2). The corresponding near-surface NO_2 VMR are obtained by dividing the NO_2 concentrations by the air number density. To derive the air number density, we use monthly averaged pressure and temperature profiles over a 20-year period. These profiles are extracted from the European Centre for Medium-Range Weather Forecasts (ECMWF) ERA-Interim reanalysis. In the last step, the tropospheric NO_2 VCD is calculated from the product of the near-surface NO_2 concentration with the MLH_{NO2}.

Regarding the aerosols, the AOD is estimated for every off-axis measurement (see Fig. 4a). The near-surface aerosol extinction is then calculated as the ratio between the aerosols inside the MLH_{NO2} (i.e., AOD times p) and MLH_{NO2}. The near-surface aerosol extinction refers to the layer that extends from the surface to the MLH_{NO2}. As mentioned above, around 30% of the total aerosols is expected to be found inside this layer.

The effect of SZA, RAA, and MLH_{NO2} on the simulated L_{NO2} is investigated in the supplement. First, the simulated L_{NO2} are presented in Fig. S1 as a function of RAA for different MLH_{NO2} and wavelengths and a single AOD and SZA value. L_{NO2} strongly depends on MLH_{NO2}. The lower the MLH_{NO2}, the shorter the L_{NO2} is. The same NO_2 concentration and aerosol load are used for the three different MLH_{NO2} scenarios. So, when aerosols are concentrated in a thin layer (i.e., MLH_{NO2}=0.5 km), L_{NO2} becomes shorter. Secondly, we observe that L_{NO2} depends on RAA. The larger the RAA, the longer the L_{NO2}. In Fig. S2, simulated L_{NO2} are plotted for each wavelength and each considered MLH_{NO2} as a function of SZA (at a constant AOD and RAA). L_{NO2} depends strongly on SZA. The highest dependency is observed for large SZA values, where L_{NO2} becomes maximum. Finally, in both Fig. S1 and S2, we observe that L_{NO2} becomes longer with wavelength, which is expected because of the less pronounced Rayleigh and Mie scattering at longer wavelengths.

An example of dual-scan MAX-DOAS retrieval is shown in Fig. 6. Based on the RTM simulations described above, L_{NO2} is derived for the wavelengths of interest, and ultimately, near-surface NO_2 concentrations and tropospheric NO_2 VCDs are estimated. In the last step, the near-surface aerosol extinction values are assigned to the six different wavelengths.
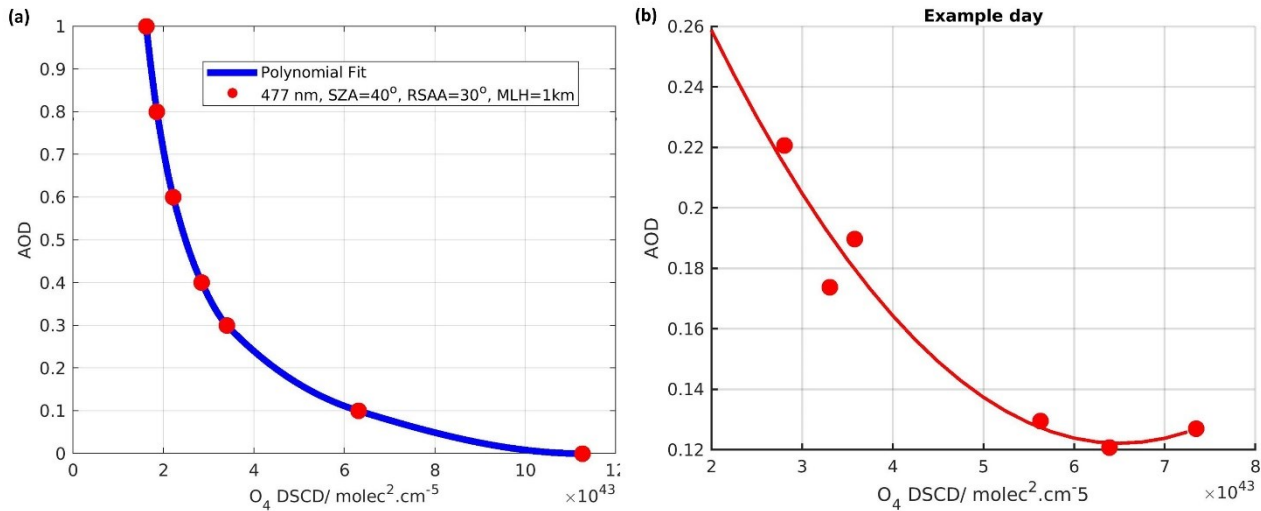
Figure 4. (a) Dots: Simulated AOD for NO₂ box profile of 1 km at 477nm for a SZA of 40° and RAA of 30° as a function of the simulated O₄ DSCDs for the different AOD values (1, 0.8, 0.6, 0.4, 0.3, 0.1 and 0; see Table 2). Blue line: simulated AOD by applying an exponential fit through the data points. (b) Dots: Estimated AOD in the six wavelengths used in the retrieval for one example day (11 September 2018). Red line: fitted line through the data points.
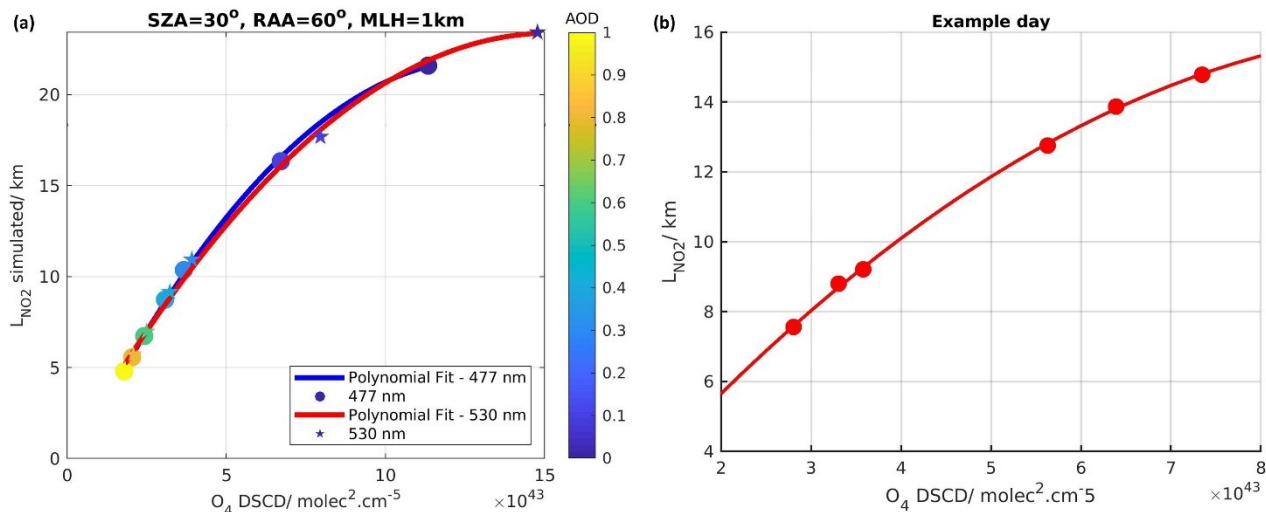
Figure 5. (a) Dots (stars): Simulated L_NO2 for NO₂ box profile of 1 km at 477nm (530 nm) for a SZA of 30° and RAA of 60° as a function of the simulated O₄ DSCDs for the different AOD values (1, 0.8, 0.6, 0.4, 0.3, 0.1 and 0; see Table 2).

Blue (red) line: 2nd-order polynomial fit through the data points. (b) Dots: Estimated L_NO2 in the six wavelengths used in the retrieval for one example day (11 September 2018). Red line: fitted line through the data points.

375

380
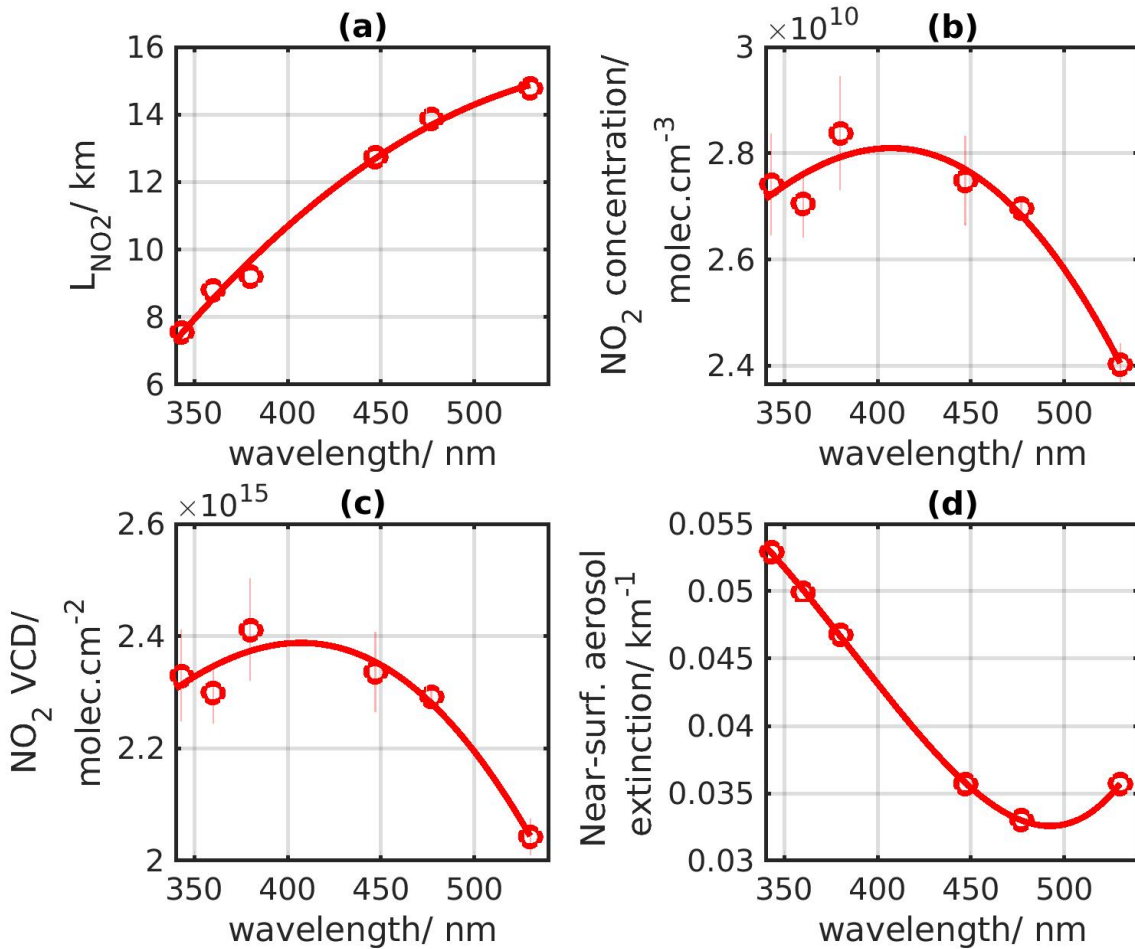
Figure 6. (a) Corresponding L_NO2, (b) near-surface NO2 concentrations, (c) NO2 VCDs, and (d) aerosol optical densities as a function of the six wavelengths used in the retrieval (11 September 2018, 11:51 UTC, 123.5º azimuthal direction).

385

4.2.2 Uncertainty budget

To estimate uncertainties on the dual-scan parameterized NO_2 near-surface concentration and VCD, the standard error propagation method is used as:

$$\sigma^2_{c_{NO_2}} = \left(\sigma_{dSCD_{NO_2}} \frac{\partial c_{NO_2}}{\partial dSCD_{NO_2}}\right)^2 + \left(\sigma_{L_{NO_2}} \frac{\partial c_{NO_2}}{\partial L_{NO_2}}\right)^2 \tag{7}$$

390

which is solved as:

$$\sigma^2_{c_{NO_2}} = \left(\frac{\sigma_{dSCD_{NO2}}}{L_{NO_2}}\right)^2 + \left(-\frac{\sigma_{L_{NO2}} dSCD_{NO2}}{L^2_{NO2}}\right)^2 \tag{8}$$

and then:

$$\sigma^2_{c_{NO_2}} = \left(\sigma_{dSCD_{NO_2}} \frac{c_{NO_2}}{dSCD_{NO_2}}\right)^2 + \left(\sigma_{L_{NO_2}} \frac{c_{NO_2}}{L_{NO_2}}\right)^2 \tag{9}$$

395

where:

$$\sigma^2_{L_{NO2}} = \left(\frac{L_{NO2}}{dSCD_{NO2(sim)}} \sigma_{dSCD_{NO2}}\right)^2 + \left(\frac{L_{NO2}}{MLH_{NO2}} \sigma_{MLH_{NO2}}\right)^2 \tag{10}$$

According to Kreher et al. (2019) and Bösch et al. (2018), in urban or suburban polluted conditions, the use of the DOAS fit
400 uncertainty of NO_2 for the $dSCD_{NO2}$ uncertainty is not appropriate, because the $dSCD_{NO2}$ uncertainty is mostly driven by atmospheric variability as well as spatial and temporal fluctuations in the O_4 and NO_2 fields. In this study, a conservative value of 3.5×10^{15} molec.cm^{-2} is attributed to $\sigma_{dSCD_{NO_2}}$ (Kreher et al., 2019). This represents an error of up to 6.0% on the NO_2 dSCDs in the visible range (477 nm).

The second error source is related to the estimation of L_{NO2} from the RTM simulations. To estimate this error, sensitivity tests
405 on the input aerosol and NO_2 vertical profiles were performed. The fraction of aerosols located inside the MLH_{NO2} (40% and 60% instead of 30%) and the NO_2 profile shape (linearly decreasing instead of box) were modified. The error related to the RTM simulations of the simulated $dSCD_{NO2}$ is about 9.6% in the Visible range (477 nm). Additionally, according to Dimitropoulou et al. (2020), the uncertainty related to MLH_{NO2} is about 4% in the Visible range (477 nm).

Combining all the error sources, the total uncertainties on the NO_2 near-surface concentration is about 12.7%, 12.4%, 11.4%,
410 11.1%, 11.3%, and 12.6% in 343 nm, 360 nm, 380 nm, 447 nm, 477 nm, and 530 nm, respectively.

Finally, the total uncertainties on the NO_2 VCD is about 12.0%, 11.7%, 10.7%, 10.3%, 10.6%, and 11.9% in 343 nm, 360 nm, 380 nm, 447 nm, 477 nm, and 530 nm, respectively.

4.2.3 Verification of the dual-scan MAX-DOAS retrieval method

415   The sanity check and verification of the dual-scan MAX-DOAS retrieval method in Uccle is based on two different correlative comparisons.

The sanity check compares the NO_2 near-surface VMRs and tropospheric VCDs retrieved by the dual-scan parameterization in the main azimuthal direction to the same quantities retrieved with the MMF inversion algorithm at the two main wavelengths (360 nm and 477 nm). As can be seen in Figures 7 and 8, both data sets are in good agreement, with correlation coefficient

420   values in the range of 0.86 to 0.95 and slope values close to unity for all the four comparisons.

The verification step is based on the same type of comparison as the first one but for three additional azimuthal directions, where elevation scans, and hence profile retrievals, are available for some periods. Onward July 3, 2019, elevation scans were performed in these three additional azimuthal directions to complement the already existing measurement set-up. These elevation scans were performed once per day, around noon, in the 11°, 105°, and 262.5° azimuthal directions. Figure 9 shows

425   the comparison between near-surface NO_2 VMRs and tropospheric VCDs retrieved by the dual-scan parameterization method and the corresponding results obtained with the MMF inversion algorithm. Overall good agreement is obtained (R=0.79 and 0.84 for near-surface VMR and VCD, respectively). We observe that the comparison concerning the near-surface NO_2 VMR seems to be noisier than in the main azimuth direction. This is mainly due to the use of the MLH_{NO2} calculated in the main azimuthal direction for all the different azimuth angles in the dual-scan method. Additionally, the parameterization technique

430   slightly underestimated the near-surface NO_2 VMR (s=0.84) while a slope value of 1.00 is obtained for tropospheric VCDs.
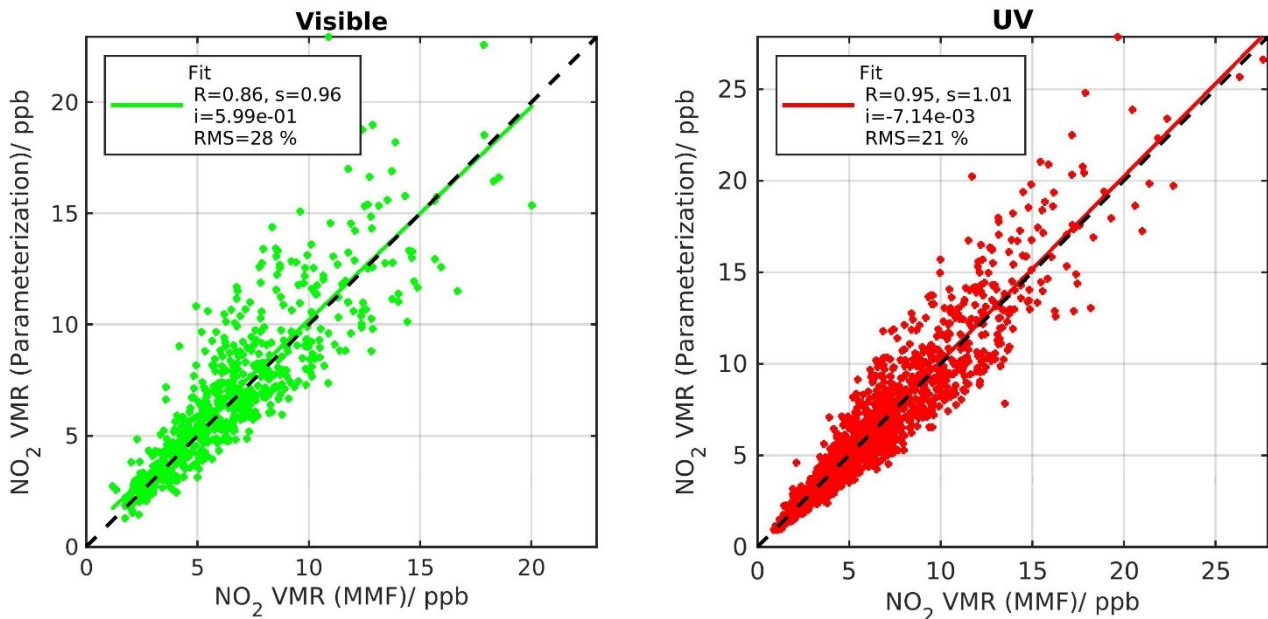
Figure 7. Comparison between MMF and parameterized NO₂ near-surface VMR at 477 nm (Visible, left panel), and 360 nm (UV, right panel), as derived from the main azimuthal direction (i.e., 35.5º azimuthal direction).

435
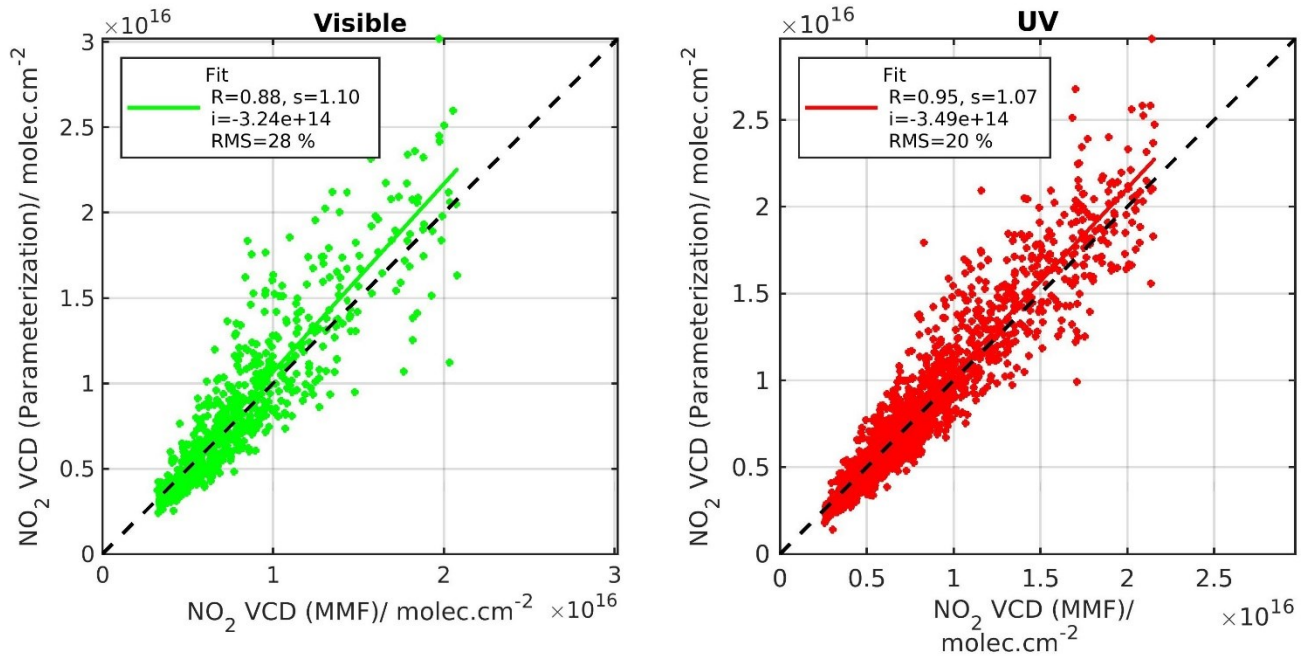
Figure 8. Comparison between MMF and parameterized NO₂ VCD at 477 nm (Visible, left panel), and 360 nm (UV, right panel), as derived from the main azimuthal direction (i.e., 35.5º azimuthal direction).
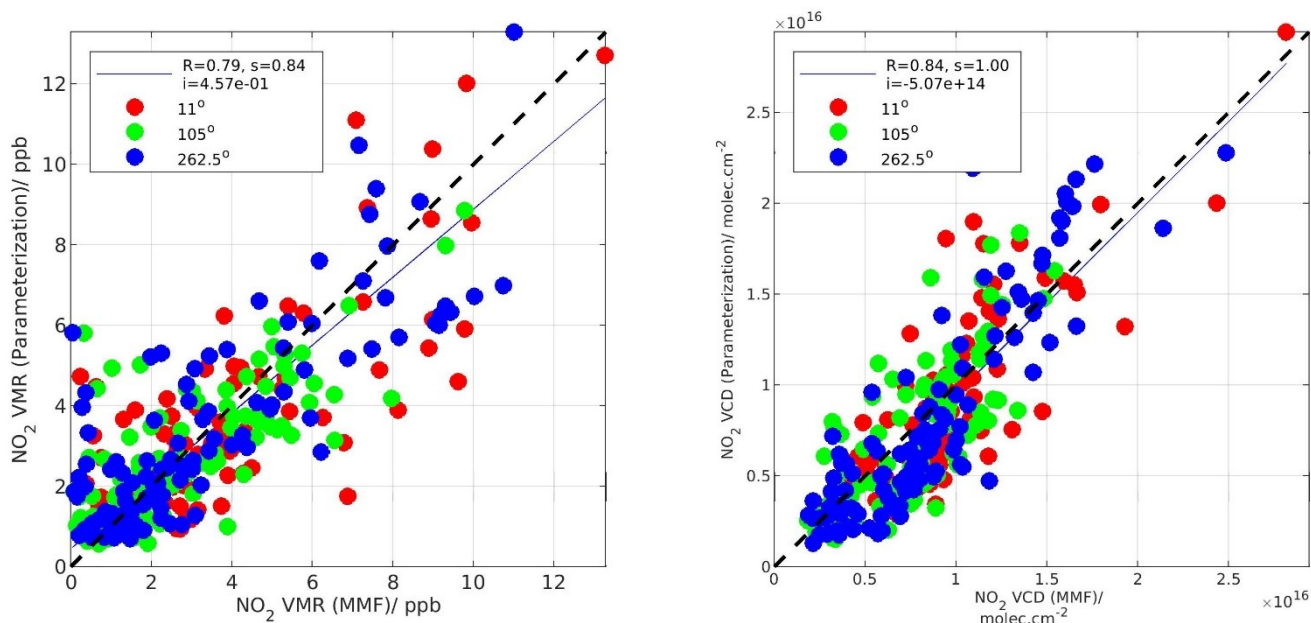
440

Figure 9. Visible range: comparison between MMF and (left panel) parameterized NO₂ near-surface VMR and (right panel) parameterized NO₂ VCD at three different azimuthal directions, as indicated in the color bar (11°, 105°, and 262.5⁰ azimuthal directions). The elevation scans in these azimuthal directions were performed once per day from 3 July 2019.

445

4.3 Horizontal distribution inversion approach

The parameterized NO₂ near-surface concentrations at the six different wavelengths are used as input in a new horizontal distribution inversion approach. As parameterized NO₂ near-surface concentrations, we refer to the conversion of the measured NO₂ dSCDs (i.e. at the elevation angle of 2°) to near-surface NO₂ concentrations by applying the dual-scan MAX-DOAS

450   retrieval method as described in Sect. 4.2. Figure 10 shows a sketch of the assumed horizontal box model configuration, in which successive boxes of concentration c_N between the horizontal distances x_{N-1} and x_N from the MAX-DOAS instrument are considered along the light path. The index N is equal to the total number of successive boxes.

The different horizontal lines illustrate the horizontal extent (or differential effective light path as described in Sect. 4.2) in which the NO₂ near-surface concentrations are extended for the six different wavelengths. Generally, the MAX-DOAS

455   horizontal sensitivities are longer for larger wavelengths because of the less pronounced Rayleigh scattering (see also Fig. 6; Ortega et al., 2016; Dimitropoulou et al., 2020). In Fig. 10, the shortest line represents the smallest wavelength's horizontal sensitivity (343 nm), and the longest line the largest wavelength's horizontal sensitivity (530 nm). As can be seen in the sketch, the effective horizontal light path at the six different wavelengths passes through different number of horizontal bins.

The parameterized NO2 near-surface concentrations at the different wavelengths are the mean concentrations along the
460   horizontal effective light paths (see Section 4.2), which are also called differential effective light paths because they are linked
to the dSCD$_{NO2}$. When having information coming from one wavelength only, it is not possible to know how the NO2 is
distributed along this light path. In the present work, the knowledge of mean NO2 concentrations at six different wavelengths
is used to retrieve a horizontal NO2 profile, assuming the horizontal box model described in Fig. 10. This new retrieval method
is described below.

465

The measurement vector **y** consists of the six retrieved surface concentrations (called as $\bar{c}_{NO2}$; see method presented in Sect.
4.2) at the six different wavelengths. These near-surface concentrations can be expressed as functions of the different effective
light paths (**L$_{NO2}$**) and correspond to the average surface concentrations along those **L$_{NO2}$**:

470   $$\mathbf{y} = \mathbf{F_{meas}}(c_{NO2\_true}) = \bar{c}_{NO2} = \frac{dSCD_{NO2}}{L_{NO2}} \tag{11}$$

F$_{calcul}$, which represents the forward model, can be expressed as follows:

$$\mathbf{F_{calcul}}(c_{NO2\_true}) = \frac{1}{L_{NO_2}} \int_0^{L_{NO2}} \mathbf{c_{NO2}}(x)dx \tag{12}$$

475   where x is the horizontal distance and c_{NO2} the NO2 near-surface concentration as a function of x, the distance from the MAX-
DOAS instrument.

Our retrieval of the horizontal distribution of $\mathbf{c_{NO_2}}$ is based on the inversion theory (Rodgers, 2000), in which a horizontal
profile c_{NO2} (state vector) is retrieved given an a-priori horizontal profile $\mathbf{x}_a$, the measurement vector **y**, the matrix of the
480   weighting function **K**, the uncertainty covariance matrix of the a priori **S$_a$** and the uncertainty covariance matrix of the
measurement **S$_e$**:

$$c_{NO2} = \mathbf{x_a} + (\mathbf{K^T S_e^{-1} K + S_a^{-1}})^{-1} \mathbf{K^T S_e^{-1}} (\mathbf{y - Kx_a}) \tag{13}$$

485   The weighting function indicates the sensitivity of the measurement vector to a change in the horizontal profile. It is given in
the present case by the following analytical functions:

$$\mathbf{K}(x, \mathbf{L_{NO_2}}) = \frac{d\mathbf{F_{calcul}}}{dc_{NO2}} = \begin{cases} \frac{dx}{L_{NO_2}} & \text{for } 0 < x < \mathbf{L_{NO_2}} \\ \frac{A\,dx}{L_{NO2}} & \text{for } x\,(max) > \mathbf{L_{NO_2}} \\ \mathbf{0} & \text{for } x > \mathbf{L_{NO_2}} \end{cases} \tag{14}$$

where A is the coverage percentage of the differential effective light path length at the last horizontal grid x (max).

490 An example of weighting functions is presented in Fig. 11. As can be seen, each measurement is sensitive from the MAX-DOAS instrument location to the horizontal distance equal to the differential effective light path length of each measurement. As each last horizontal grid is not fully covered by each measurement, the coverage percentage is considered for these grid cells. It should be noted that since NO_2 is an optically thin absorber, the measurements depend linearly on each horizontal box's concentration. For this reason, OEM for the linear case is considered here, and only one inversion step is needed (see

495 Eq. 13).

The selected output horizontal grid for the retrieval extends from the MAX-DOAS instrument to the maximum differential effective light path (L_{NO2} at 530 nm) per azimuthal direction and consists of successive boxes of 0.5 km thickness on the horizontal axis.

Since this inversion problem is ill-conditioned, more than one horizontal NO_2 profile can be consistent with the measurement

500 vector. To reject unrealistic solutions, the a priori profile $\mathbf{x_a}$ and its uncertainty covariance matrix must be included in the retrieval. In the OEM, the a priori information usually comes from an independent source, like a model or other correlative measurements. In the present study, RIO model data were chosen as a priori. RIO is a land-use regression model based on the interpolation of the hourly NO_2 near-surface concentrations measured by the in-situ telemetric air quality network in Belgium (Hooyberghs et al., 2006; Janssen et al., 2008). RIO provides hourly NO_2 concentration maps on a 4x4 km^2 spatial resolution.

505 Seasonal average maps of RIO NO_2 near-surface concentration are constructed (see Fig. S3) and after, seasonal averages of RIO NO_2 near-surface concentration horizontal profiles were calculated in each azimuthal direction and interpolated on the retrieval's horizontal grid by regridding the initial 4x4 km^2 spatial resolution to a finer one (see Fig. 12). The shape of the RIO a priori NO_2 profiles per azimuthal direction stays the same during different seasons of the year, indicating that the wind effect on NO_2 transportation disappears by the seasonal averaging and that the same sources contribute to the NO_2 horizontal field.

510 A mean scaling factor equal to the mean ratio between the measured and RIO NO_2 near-surface concentrations is applied because of the systematic underestimation of NO_2 near-surface concentrations by MAX-DOAS when compared to in-situ measurements (see Dimitropoulou et al., 2020 and Section S1).

For the aerosols horizontal distribution retrieval, there are not sufficient independent measurements that provide information about the horizontal distribution of AOD and can serve as an a priori AOD profile. Therefore, a linearly decreasing a priori

515 AOD profile is used in the AOD retrieval based on CIMEL observations. An AOD equal to 0.18, which is the yearly-averaged AOD value from CIMEL at 477 nm, is used close to the MAX-DOAS instrument with a linear decrease as we move away from the instrument. To construct the near-surface aerosol extinction a priori profiles, it is considered that 30% of the total amount of AOD is located inside the MLH (i.e., known for each MAX-DOAS vertical scan from the MMF inversion algorithm; see Section 4.1).

520 The diagonal elements of the $\mathbf{S_a}$ matrix are set equal to the square of a scaling factor times the NO_2 concentration a priori profile. The non-diagonal elements, which account for correlation between the different horizontal grid cells, are set as follows (Barret et al., 2002):

$$S_{a_{ij}} = \sqrt{S_{a_{ii}}S_{a_{ij}} \exp\left(-\ln(2)\left(\frac{x_i-x_j}{\gamma}\right)^2\right)} \qquad (15)$$

where x_i and x_j are the horizontal distances at the ith, and j^{th} horizontal boxes and γ is half of the correlation length. γ is set equal to 3.5 km. To eliminate inversion instabilities, S_a elements which are smaller than 0.1% of the maximum S_a element are set equal to zero.

To estimate the correlation length, a covariance matrix was constructed by exploiting the airborne observations above Brussels (28 June 2019). The airborne observations have a spatial resolution of approximately 100 x 100 m^2. NO$_2$ horizontal profiles were constructed in different azimuthal directions in a spatial resolution of 500 x 500 m^2, expanding from the MAX-DOAS's position to a maximum distance of 20 km, and were used to calculate a covariance matrix. A correlation length equal to 7 km, and consequently, a gamma value equal to 3.5 km, is found to be representative for the NO$_2$ horizontal profiles in Brussels. Using this correlation length, a variance of 45% is used. This choice was conducted based on the seasonal variance of the RIO a priori profiles compared to their seasonal mean value. It is found that the seasonal variance of RIO observations has a mean value of 45%. Additionally, it is found to be a good compromise for obtaining reasonable retrieval results e.g. in terms of information content, and while avoiding unrealistic oscillations in the retrieved aerosol and NO$_2$ profiles.

The measurement covariance matrix S_e is chosen to be diagonal, with elements corresponding to the uncertainties of the dual-scan parameterized NO$_2$ near-surface concentration (see Section 4.2.2).

Three examples of the retrieved NO$_2$ horizontal profile are presented in Fig. 13, together with corresponding measured and simulated $\overline{c}_{NO2}$ at the six different wavelengths for July 2, September 11, and September 30 2018 RMS is calculated between measured and simulated NO$_2$ near-surface concentrations of the horizontal retrieval normalized by the mean of the measured NO$_2$ near-surface concentrations (upper panels in Fig. 13). For distances smaller than the minimum L_{NO2} (around 8 km), the measurements do not give information about the horizontal distribution of NO$_2$. Consequently, the retrieved NO$_2$ horizontal profile at these ranges is coming from the a priori profile. Similarly, the measured and retrieved near-surface aerosol extinction coefficient and the retrieved aerosol horizontal profile are shown in Fig. 14, for three sample cases..

An essential condition of the dual-scan MAX-DOAS retrieval and the new horizontal inversion approach at six different wavelengths is the increasing trend of the horizontal sensitivity as a function of wavelength. Consequently, every wavelength is sensitive to a different horizontal region and the six different wavelengths can be used to retrieve the horizontal distribution of aerosols and trace gases. Sensitivity tests were conducted in which simulated L_{O4} are expressed as a function of the six different wavelengths for different aerosol conditions. As can be seen in Fig. S4, the linear relationship between L_{O4} (and L_{NO2}) and wavelength exists for AOD values ranging from 0 to 1. An AOD equal to unity is chosen as the maximum AOD of the simulations because in Uccle, AOD values rarely exceed one (see in https://aeronet.gsfc.nasa.gov/ for the Brussels measurement site). Therefore, the relation stays linear as the aerosol load changes for the conditions observed in Uccle. The

555   only condition leading to non-linearity is when clouds are present. However, as explained in Sect. 4.1, a cloud filtering

approach is applied, rejecting the broken cloud scenes, which are the more problematic ones.
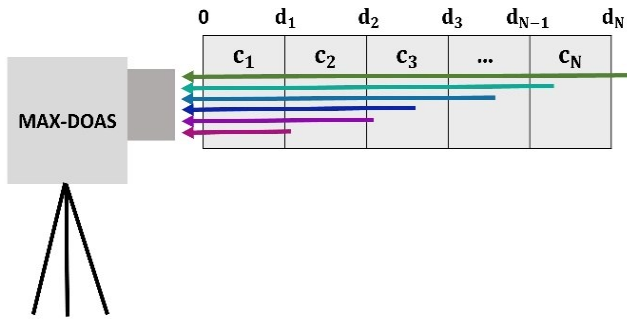
560   **Figure 10. Schematic representation of the six different L_{NO2} (i.e., one horizontal line for each wavelength) used in the new horizontal distribution inversion approach. The length of each line shows the sensitivity of each wavelength as a function of the horizontal distance. The shortest line represents the smallest wavelength.**

565
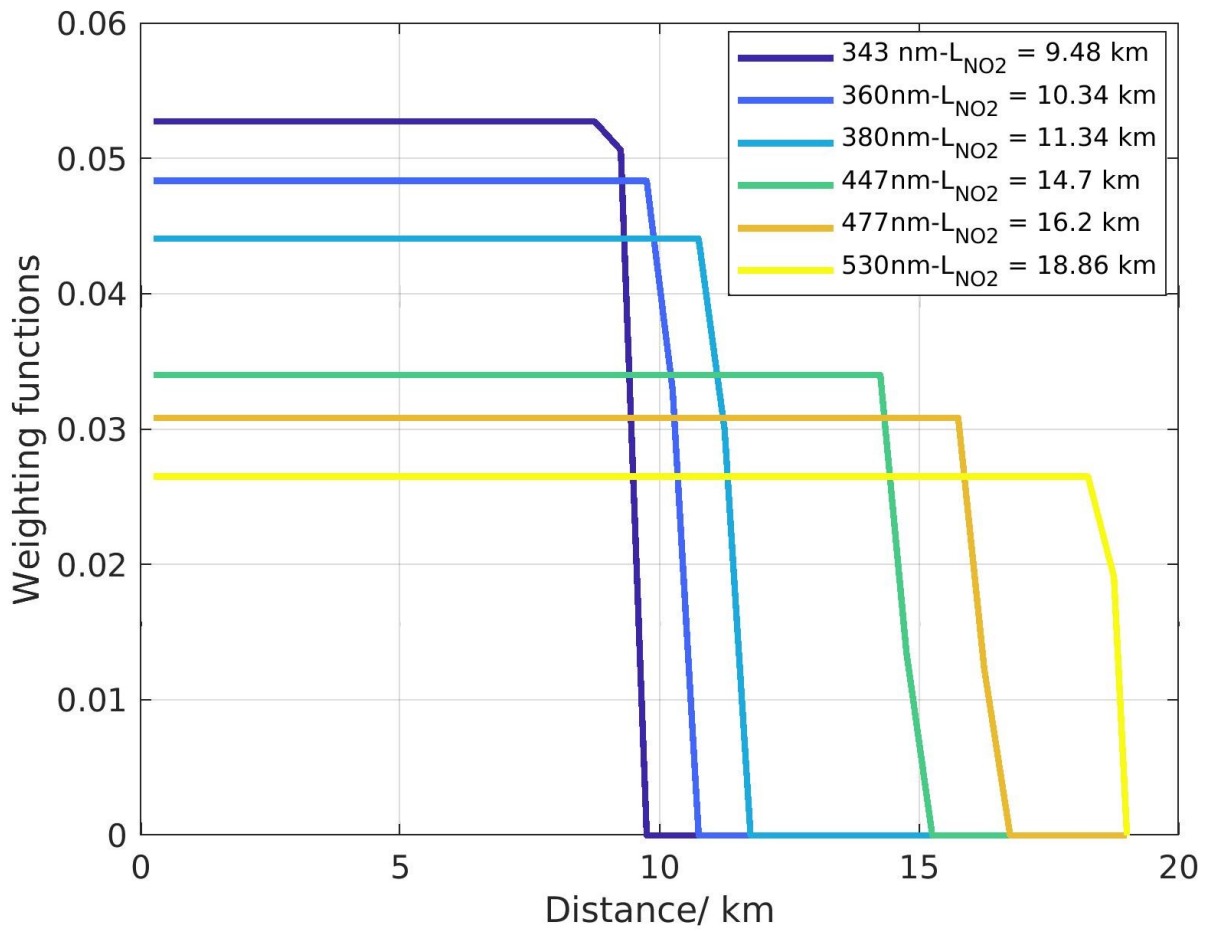
Figure 11. Examples of weighting functions used in the new horizontal distribution inversion approach (11 September 2018, 11:26 UTC).

570

575
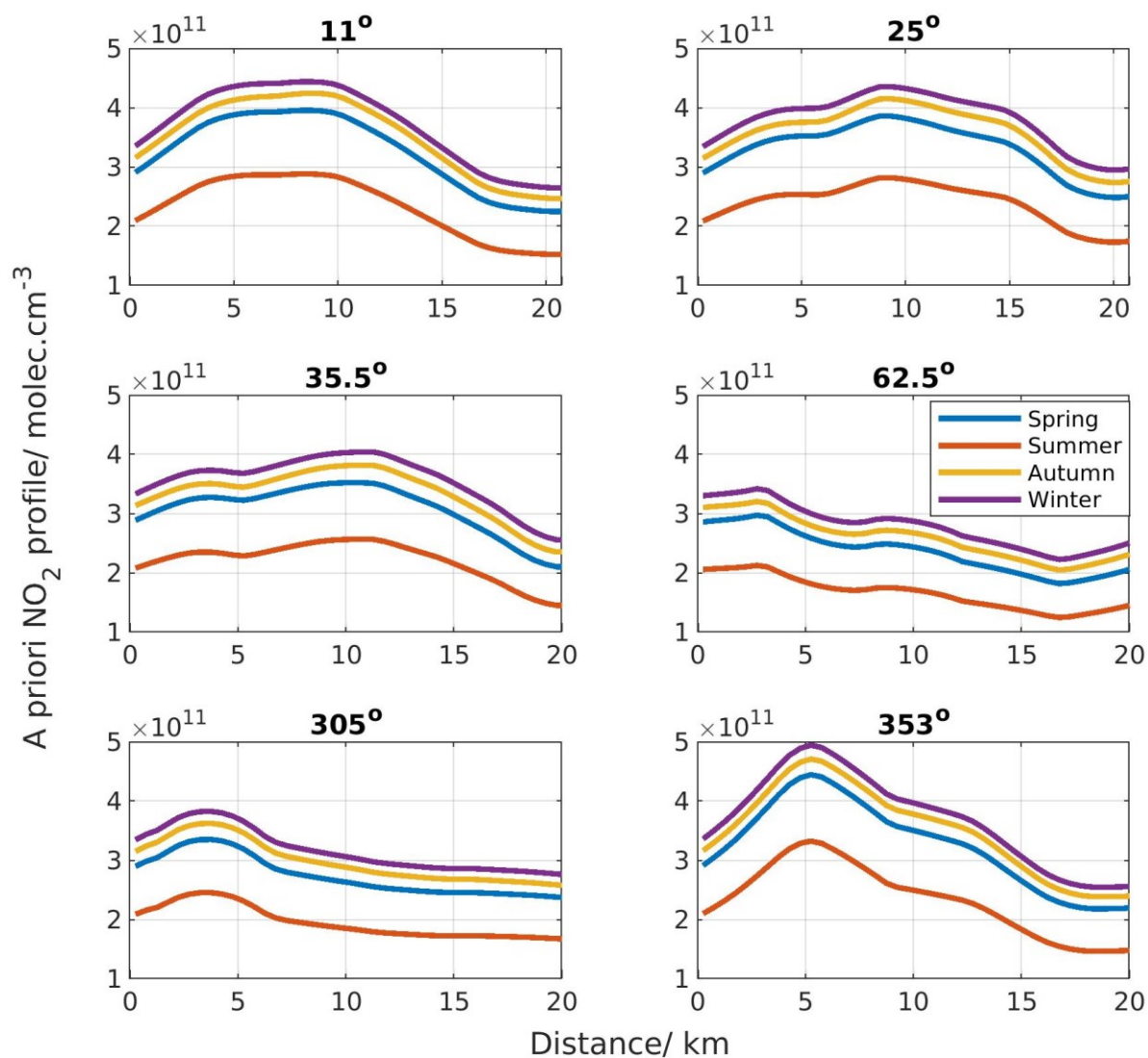
Figure 12. Example of seasonal RIO *a priori* NO₂ horizontal profiles for the new horizontal distribution inversion approach as a function of the horizontal distance from the MAX-DOAS instrument in six different azimuthal viewing directions, before the application of the scaling factor.
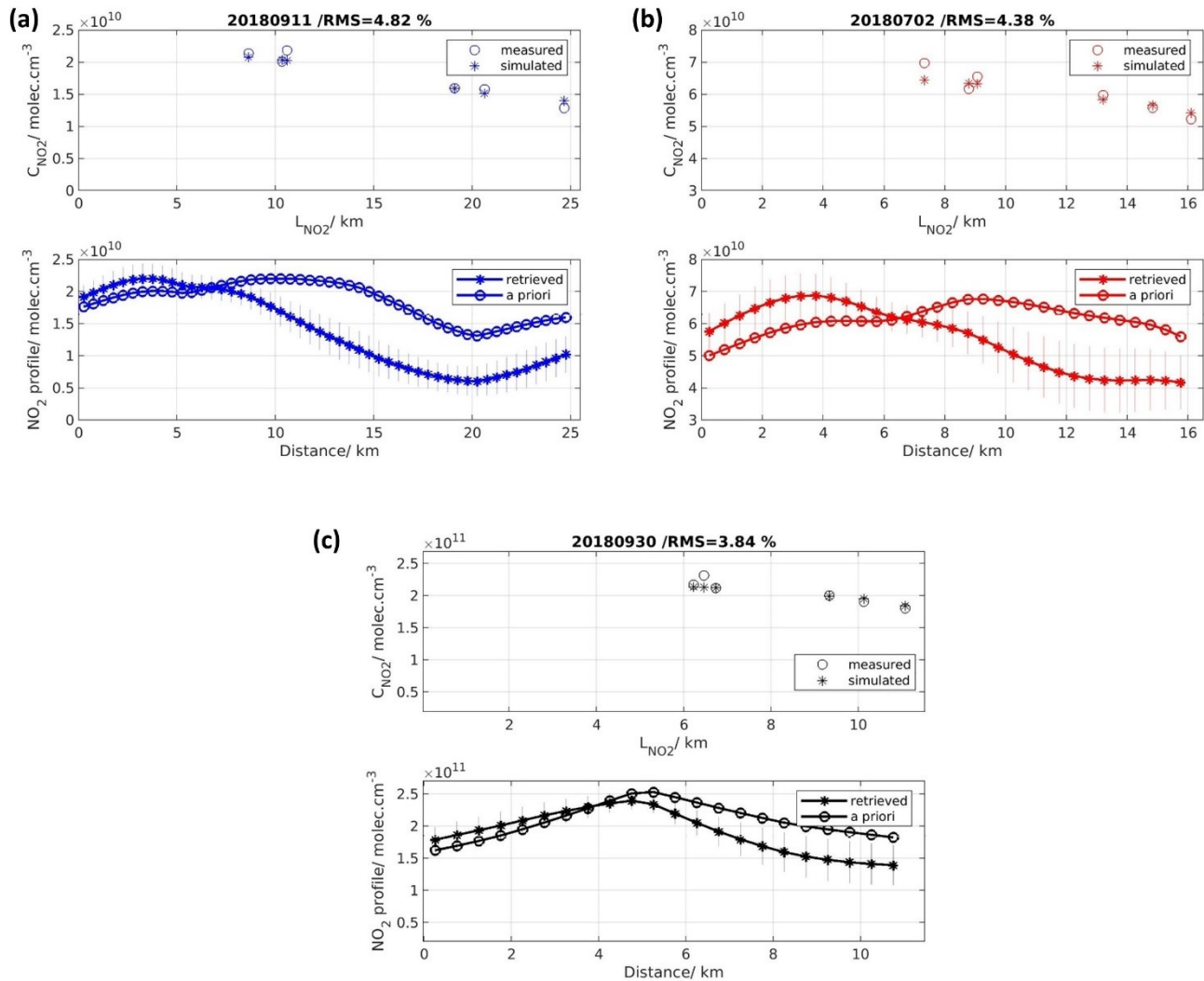
Figure 13. (Upper panels in a, b, and c) Measured and retrieved NO₂ near-surface concentrations at the six different wavelengths (i.e., horizontal distances) as a function of the estimated horizontal distances and (lower panels in a, b, and c) the retrieved NO₂ near-surface horizontal profile and a priori profile. The two panels correspond to the (a) 11 September 2018, 12.91 UTC, 265º azimuthal direction, (b) 02 July 2018, 10.42 UTC, 25º azimuthal direction, and (c) 30 September 2018, 07.96 UTC, 167.5º azimuthal direction.
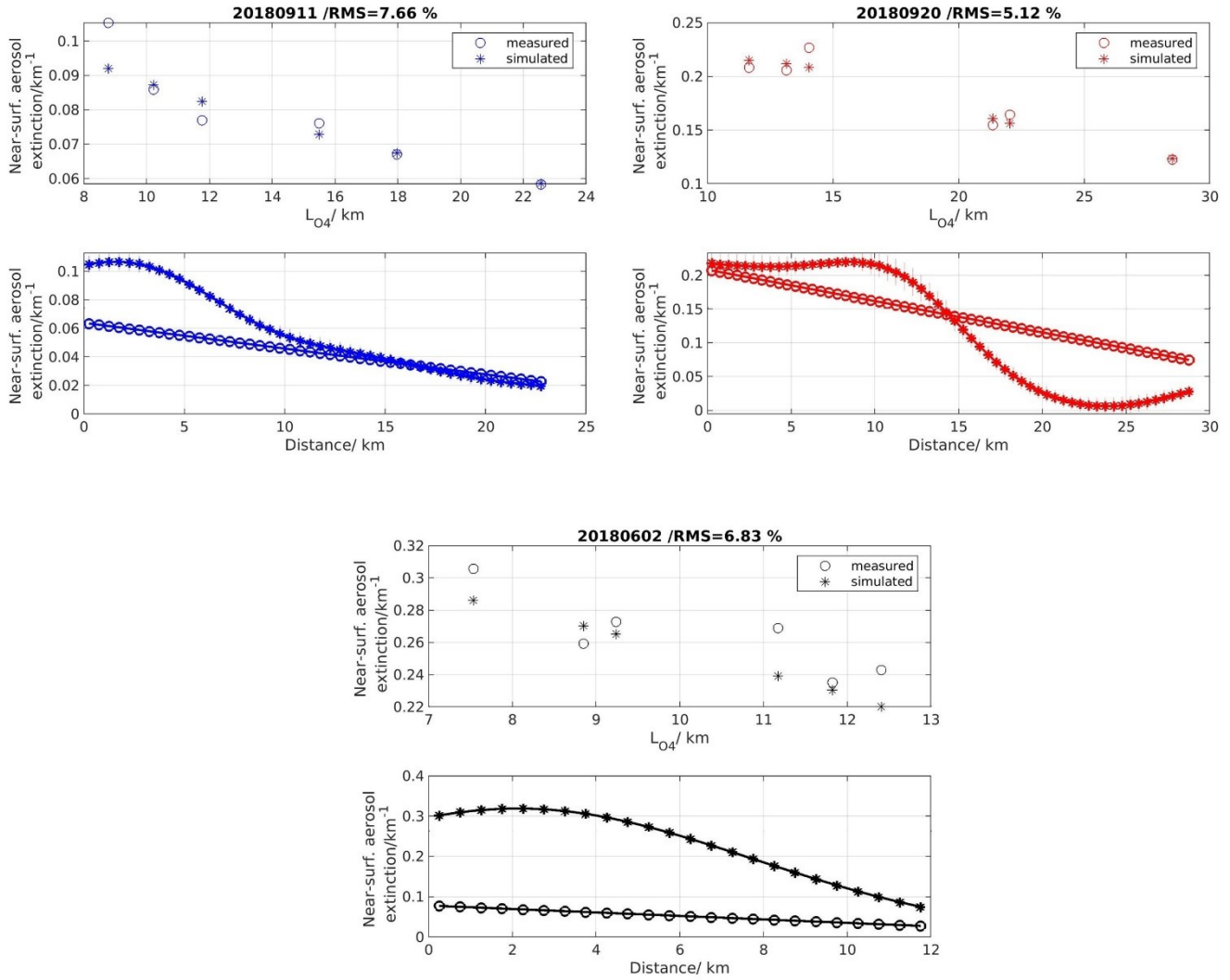
Figure 14. (Upper panels in a,b, and c) Measured and retrieved near-surface aerosol extinction at the six different wavelengths (i.e., horizontal distances) as a function of the estimated horizontal distances and (lower panels in a, b, and c) the retrieved near-surface aerosol extinction horizontal profile. The two panels correspond to the (a) 11 September 2018, 11.48 UTC, 167.5º azimuthal direction, (b) 20 September 2018, 07.08 UTC, 25º azimuthal direction, and (c) 02 June 2018, 18.16 UTC, 35.5º azimuthal direction.

4.4 Characterization of the retrieval

To characterize the retrieval, the averaging kernels, **AK**, play a crucial role. The **AK** matrix is calculated as follows (Rodgers, 2000):

610

$$AK = \frac{dc_{NO2}}{dc_{NO2\_true}} = (K^T S_e^{-1} K + S_a^{-1})^{-1} K^T S_e^{-1} K \tag{16}$$

The **AKs** are the rows of the **AK** matrix. They present the sensitivity of the retrieved (c_{NO2}) on the true (c_{NO2_true}) atmospheric profile. Ideally, the **AK** matrix should be an identity matrix. In Fig. 15, an example of selected **AKs** is shown. As can be seen,
615 for distances smaller than the first measurement (e.g., near-surface NO_2 concentration retrieved at 343 nm), the **AKs** are constantly zero (or have small values) from the MAX-DOAS instrument until these distances. This indicates a low sensitivity on these short distances, and therefore information about the horizontal distribution of NO_2 is coming essentially from the a priori profile. The **AKs** create a maximum flat plateau close to their nominal horizontal distance for larger distances (d=8.75 km, d=10.25 km, and d=24.75 km). For this particular example, the **AKs** do not exceed the values of 0.06.
620 Another important information about the retrieval is the trace of the **AK** matrix, which refers to the number of degrees of freedom for signal (DOFS). The DOFS are an indication of the number of independent pieces of information that one can retrieve from the measurements. Ideally, the DOFS would be equal to the number of horizontal boxes for the horizontal distribution. In reality, the DOFS are lower, because of the limited horizontal resolution of the measurements. In Fig. 15, the DOFS are close to two, which means that two independent pieces of information are contained in the measurements for this
625 particular example.

In the present work, the total retrieval error is equal to the error related to the measurement noise and the smoothing of the true atmospheric profile. According to Rodgers (2000), the retrieval noise error is estimated as:

630 $$S_{meas} = GS_e G^T \tag{17}$$

with, G being the gain matrix:

$$G = (K^T S_e^{-1} K + S_a^{-1})^{-1} K^T S_e^{-1} \tag{18}$$

The smoothing error is calculated as follows:

$$S_{smooth} = (AK - I)S_x(AK - I)^T \tag{19}$$

635 with S_x being a realistic covariance metric of the true NO_2 horizontal profile.

The horizontal profiles of the measurement and smoothing error in percentage are shown in Fig. 16. As can be seen, the measurement error becomes maximum for the longest distance.

To eliminate the unsuccessful retrievals, the percentage of accepted retrievals with respect to the total number of retrievals
640   during the four seasons is investigated when a specific filtering on RMS and DOFS is applied (see Table 3 and Figures S7 and S8). As we can see in Fig. S8, DOFS are in the range of 1.2-2.5. From these tests, it is found that most of the retrievals have DOFS larger than 1.5 (see Fig. S8). RMS is defined as the root-mean-square deviation between measured and simulated c_{NO2} normalized by the mean of the measured c_{NO2} (e.g., same RMS as in Fig.13). Table 3 and Fig. S7 indicate that RMS values are in the range of 0-30% and most of the retrievals have an RMS smaller than 6% with a median RMS value of around 4.5%
645   during all seasons. Based on these investigations, DOFS>1.5 and RMS<6% are used as retrieval quality control criteria.

Table 3. Seasonally averaged root-mean-square (RMS) and DOFS values. RMS is calculated between measured and retrieved NO$_2$ near-surface concentrations of the horizontal retrieval (Fig. 13). DOFS represent the degrees of freedom
650   **of the horizontal retrieval (Fig. 15). The percentage of the accepted retrievals is presented for the different selection criteria.**

Season	Spring	Summer	Autumn	Winter
Median RMS (%)	3.8	4.7	4.7	4.8
Median DOFS	1.7	1.7	1.6	1.6
Accepted retrievals (%) (DOFS>1.5)	90	91	81	78
Accepted retrievals (%) (RMS<6%)	87	72	70	73
Accepted retrievals (%) (RMS<5%)	75	57	55	55
Accepted retrievals (%) (RMS<4%)	56	33	36	32
Accepted retrievals (%) (RMS<3%)	27	11	15	11
Total accepted retrievals (%) (DOFS>1.5 & RMS<6%)	80	67	57	57

655
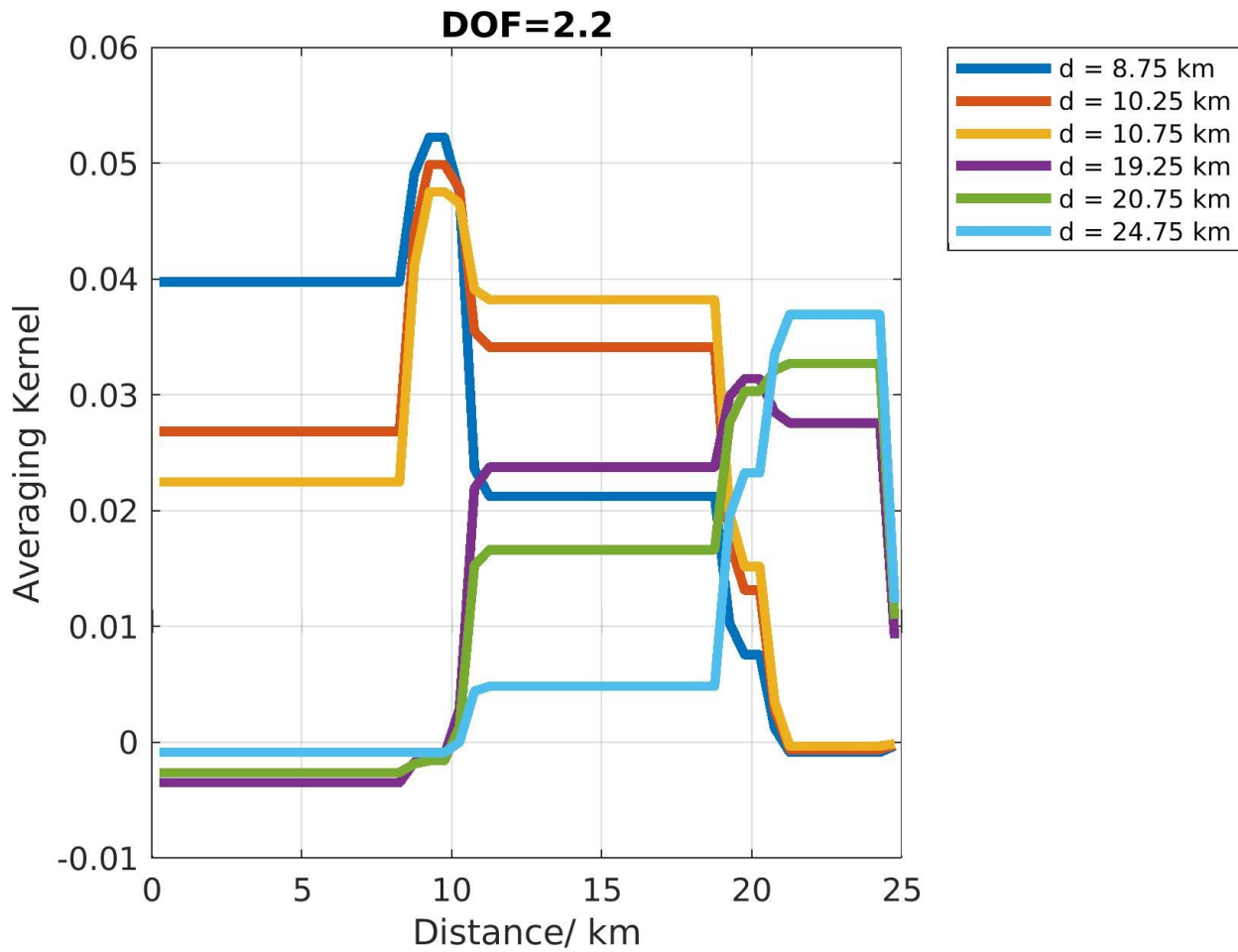
660 **Figure 15. Example of NO₂ averaging kernels. They are calculated for observations on 11 September 2018 at 11:51 UTC and 300º azimuthal direction.**

665
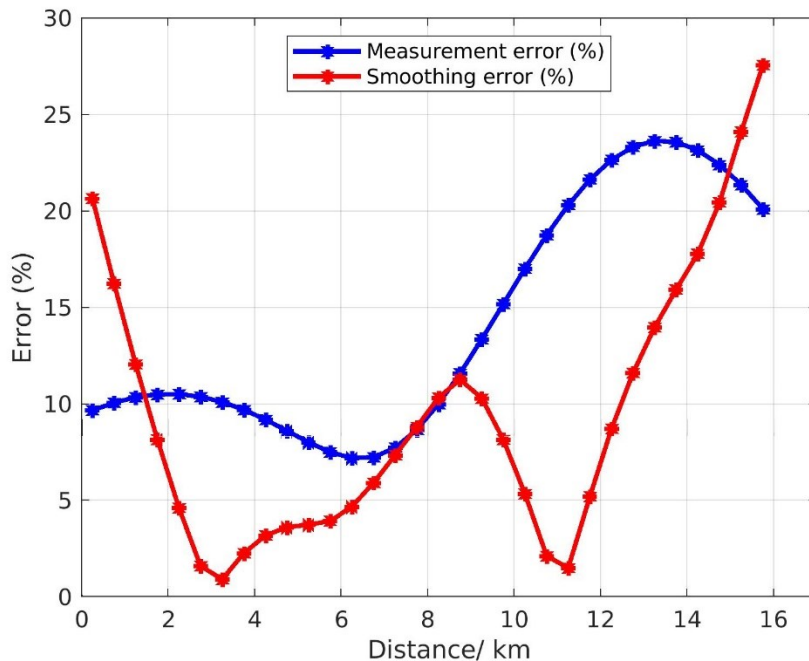
Figure 16. Example of the NO₂ measurement error in percentage for the 02 July 2018 at 10.42 UTC and 25° azimuthal direction.

 5 Retrieval results and discussion

5.1 Example of daily horizontal NO$_2$ distribution

The variation of the MAX-DOAS horizontal distribution of tropospheric NO₂ VCDs as a function of time over the course of June 28 2019, is presented in Fig. 17. This particular day is chosen because airborne measurements took place above the Brussels region (see Sect. 5.2). The horizontal NO₂ profiles are plotted per azimuthal direction with the horizontal axis showing
 the time in UTC and the vertical axis the horizontal distance in km. Because of the quality check on the retrieved NO₂ horizontal profiles (see Sect. 4.3), some profiles were rejected (e.g. azimuthal direction equal to 262.5° and 265°).

During this day, maximum NO₂ columns are mainly observed around 05:00 UTC and 10:00 UTC, which correspond to 7am and noon local time. Early in the morning (05:00 UTC), high NO₂ columns are expected to be observed because of the low MLH (MLH$_{NO2}$ in the range of 300 – 600 m height) in combination with the morning rush hour NO₂ emissions. Around 10:00
 UTC, the maximum NO₂ columns are detected in the north (N), northeast (NE), and northwest (NW) direction (see Fig. 18). Same NO₂ horizontal distribution is found when investigating the NO₂ near-surface concentrations for this day (see Fig. S5). In the Brussels region, the main emission sources are located in the N and west (W) parts of the city and are linked to the motorway around Brussels (the so-called Ring), the Brussels city center, and the Drogenbos power plant (NW direction). Concerning the NO₂ peaks, they are located at a distance around 0 to 8 km from the measurement site. It can be seen from Fig.

685   18 that the Ring, the Brussels city center, and the Drogenbos power plant are located within these distances. As measured by the meteorological station on the BIRA-IASB rooftop, the wind was coming from the E direction during that day, resulting in the progressive displacement of the NO_2 peak from the NNE to the W direction. On the contrary, the azimuthal directions pointing towards a large forested area (i.e., 62.5°, 75°, and 105°), the Bois de la Cambre, detect considerably lower NO_2 columns than the other directions.

690   Maximum near-surface aerosol extinction coefficient values are observed during all day long and detected in the N, NW and NE direction (see Fig. S6). NO_2 and aerosol peaks are co-located towards the N and NW direction.

695
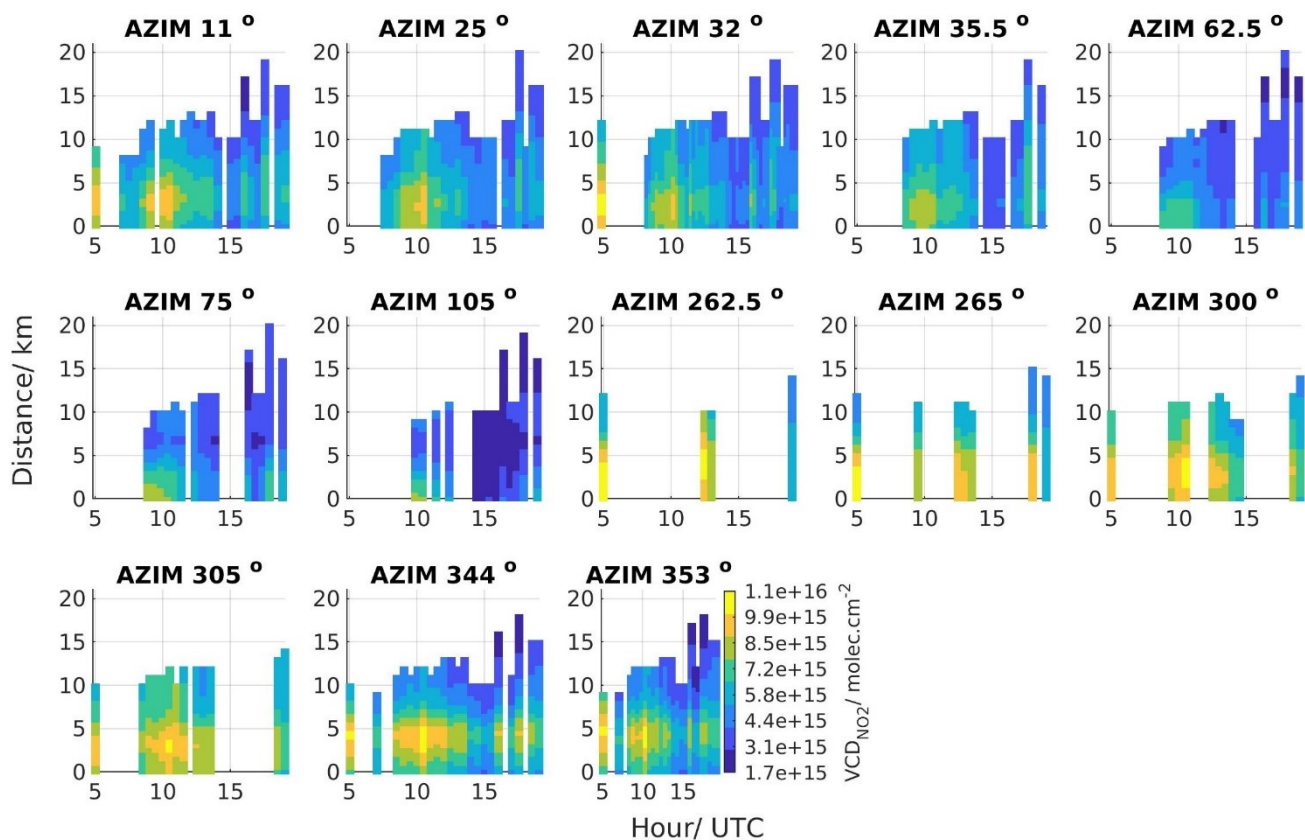
Figure 17. Diurnal variation of the retrieved NO₂ horizontal profiles per azimuthal direction as a function of time (UTC) for June 28, 2019.

700
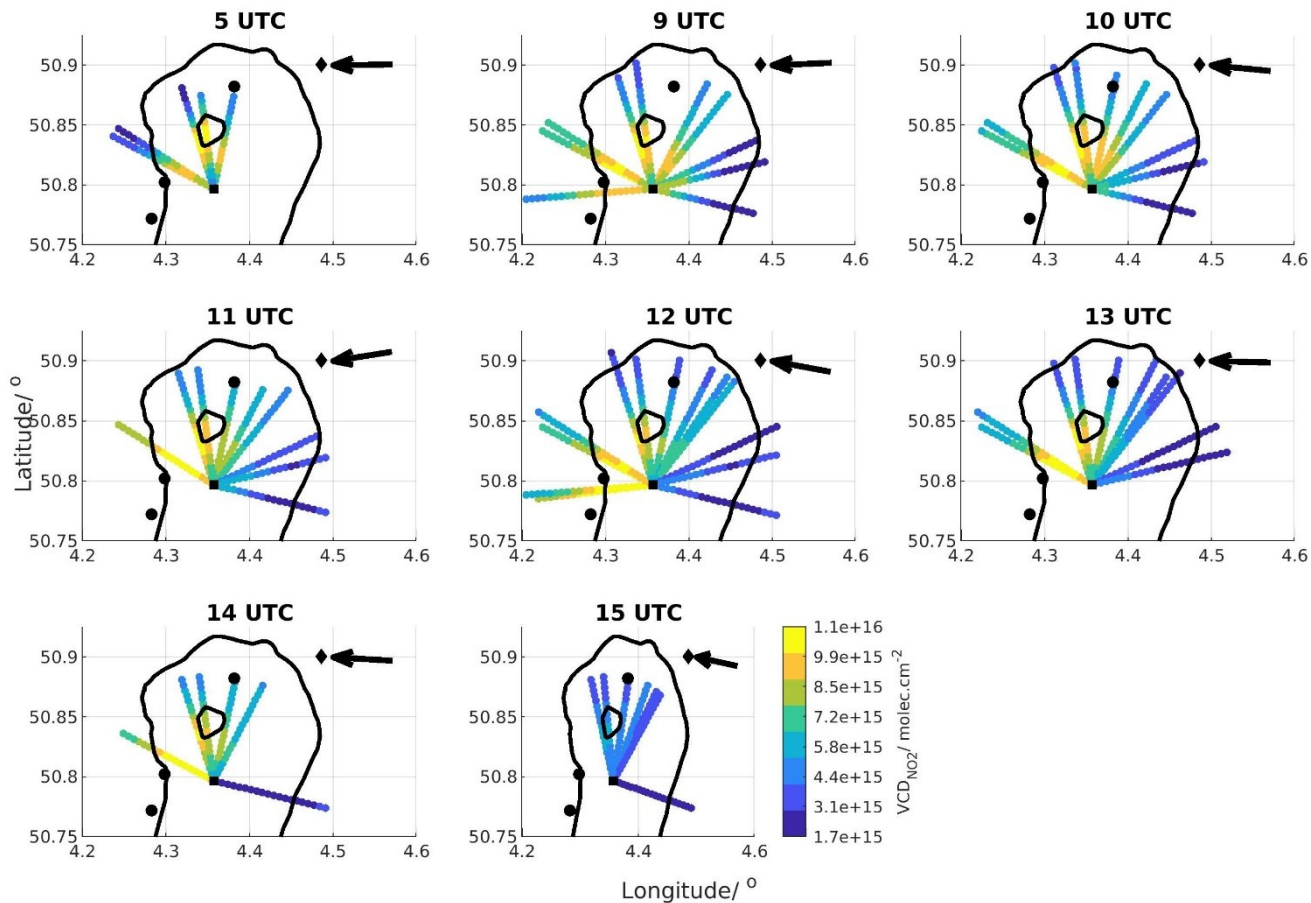
Figure 18. Maps of hourly averaged NO₂ horizontal profiles per azimuthal direction for June 28, 2019 corresponding to Fig. 17. The wind direction is shown with the black arrow. The black square shows the MAX-DOAS instrument location, the black polygon the National Airport, the black dots the NO₂ hotspots emitting more than 10 kg of NOₓ per hour (Emission Inventory of the Belgian Interregional Environment Agency, 2017) , and the black line represents the Brussels Ring road.

5.2 MAX-DOAS horizontal NO₂ distribution versus airborne, car mobile-DOAS, and TROPOMI: 28 June 2019 case study

For the S5P validation campaign over Belgium (S5PVAL-BE, https://s5pcampaigns.aeronomie.be/), airborne measurements of the two largest urban regions over Belgium, i.e., Antwerp and Brussels, took place from 26 to 29 June 2019 (Tack et al., 2021). The Airborne Prism EXperiment (APEX) imaging spectrometer was used to measure the horizontal distribution of tropospheric NO_2 columns with a spatial resolution of approximately 75 m x 120 m (Tack et al., 2017; Tack et al., 2019).

The APEX tropospheric NO_2 columns are compared to the tropospheric NO_2 horizontal distribution as retrieved by applying our new mapping MAX-DOAS technique to the 28 June 2019 measurements. During the same day, TROPOMI pixels (OFFL 010302 product; see Table 1) selected over the Brussels region are compared to MAX-DOAS observations. During this day, the TROPOMI overpass time was at 12:19 UTC. MAX-DOAS horizontal profiles of tropospheric NO_2 VCDs are selected around TROPOMI overpass time (±1 hour). The horizontal profile of MAX-DOAS NO_2 VCDs on each horizontal line-of-sight has a horizontal sampling of 0.5 km (see Fig. 13). The MAX-DOAS NO_2 VCDs on the horizontal segment crossing a TROPOMI pixel and located inside the pixel are averaged and compared to the corresponding TROPOMI NO_2 VCD. It should be noted that the MAX-DOAS segments are weighted by their relative length inside each pixel. APEX observations located inside each TROPOMI pixel were used to assign one APEX NO_2 VCD value per pixel. Maps of co-located TROPOMI, AEROMOBIL, averaged MAX-DOAS, and averaged APEX NO_2 VCDs for the 28 June 2019 are shown in Fig. 19. Two maps of APEX and MAX-DOAS observations are presented: one with APEX and MAX-DOAS in their initial resolution and one with spatially averaged APEX and MAX-DOAS observations in the area covered by a TROPOMI pixel. The NO_2 plume as detected by APEX is covering the NW, N, and NE parts of the Brussels region. MAX-DOAS successfully detected the same NO_2 plume in the NW and N but not in the NE direction. The correlation and agreement between APEX and MAX-DOAS observations is very good (R=0.84 and s=1.15). As we can observe in Fig. 20, the APEX tropospheric NO_2 VCDs tend to be larger than the MAX-DOAS ones, with an intercept equal to -2.36x10^{15} molec.cm^{-2}.

During the S5PVAL-BE flight over Brussels, car mobile-DOAS observations were performed by the BIRA-IASB mobile-DOAS, the so-called AEROMOBIL (Merlaud, 2013). The AEROMOBIL consists of a compact double Avantes spectrometer recording simultaneously scattered light in two elevation angles (i.e., one at 30° elevation angle and one at zenith). The AEROMOBIL was used to measure the spatial distribution of tropospheric NO_2 columns mainly over the Ring road of Brussels with start measurement time at 8:30 UTC and end time at 15:42 UTC. The AEROMOBIL NO_2 VCDs, which are located closest both in time and space to each MAX-DOAS horizontal grid are compared to the corresponding MAX-DOAS VCDs (see Fig. 19c and 19e). AEROMOBIL and MAX-DOAS agree perfectly on the location of maximum (i.e. NW direction) and minimum (i.e. SE direction) NO_2 tropospheric VCDs (Fig. 19c and 19e). We can observe in Fig. 20b, that the correlation coefficient is moderate (R equal to 0.74) and the slope value is equal to 0.55. The correlation plot between both datasets reveals that AEROMOBIL gives higher NO_2 tropospheric VCDs compared to MAX-DOAS ones. This finding could be partly

explained by the fact that AEROMOBIL follows busy routes, where the NO_2 tropospheric VCDs reach maximum values because of the contribution of NO_2 production resulted by vehicles' engines via fossil fuel combustion.

During the TROPOMI overpass (i.e., 12:19 UTC) above the Brussels-Capital Region, dual-scan MAX-DOAS tropospheric NO2 columns are retrieved, as it can be seen in Fig. 18. The correlation between TROPOMI and MAX-DOAS tropospheric NO_2 columns during the day of the airborne measurements above Brussels is presented in Fig. 20c. Excellent agreement is obtained, with a correlation coefficient value equal to 0.81. The slope value is equal to 0.69. During that day, MAX-DOAS and TROPOMI are in good agreement but TROPOMI tends to underestimate the tropospheric NO_2 columns. It should be noted that during that day, the range of observed NO_2 VCDs is from $3.4x10^{15}$ to $8.0x10^{15}$ molec.cm^{-2}, as retrieved by the MAX-DOAS observations.
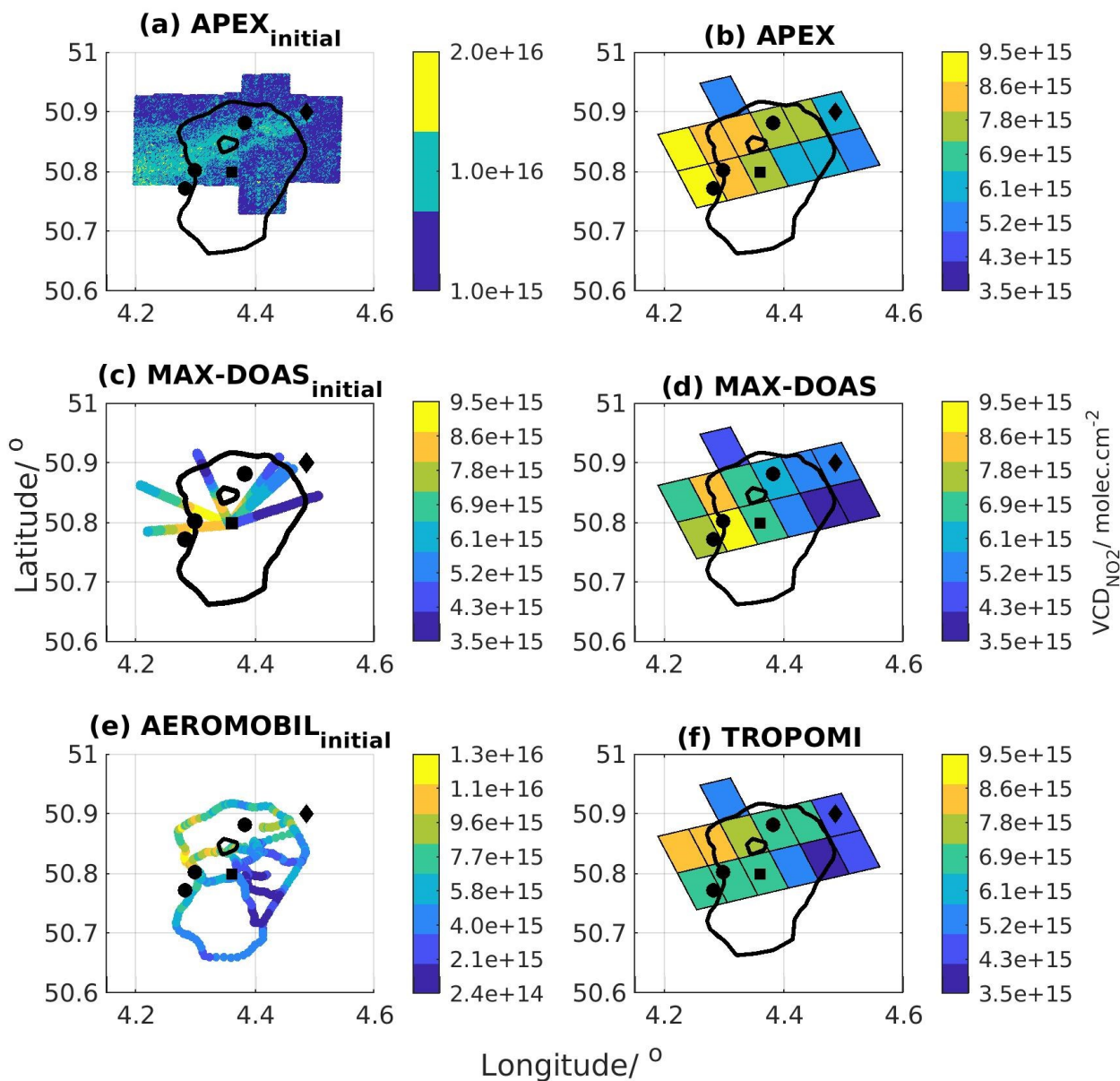
Figure 19. (a) Tropospheric NO₂ VCD as detected by the APEX instrument in its initial spatial resolution. Tropospheric NO₂ VCD maps (TROPOMI pixels) as retrieved over Brussels on 28ᵗʰ of June 2019 by the (b) APEX, (d) MAX-DOAS and (f) TROPOMI (overpass time at 12:19 UTC) instruments. Tropospheric NO₂ VCD as retrieved by the (c) MAX-DOAS and (e) AEROMOBIL (between 8:30 UTC and 15:42 UTC) in its initial spatial resolution. The black square shows the MAX-DOAS instrument location, the black polygon the National Airport, the black dots the NO₂ hotspots

emitting more than 10 kg of NO_x per hour (Emission Inventory of the Belgian Interregional Environment Agency, 2017) , and the black line represents the Brussels Ring road.
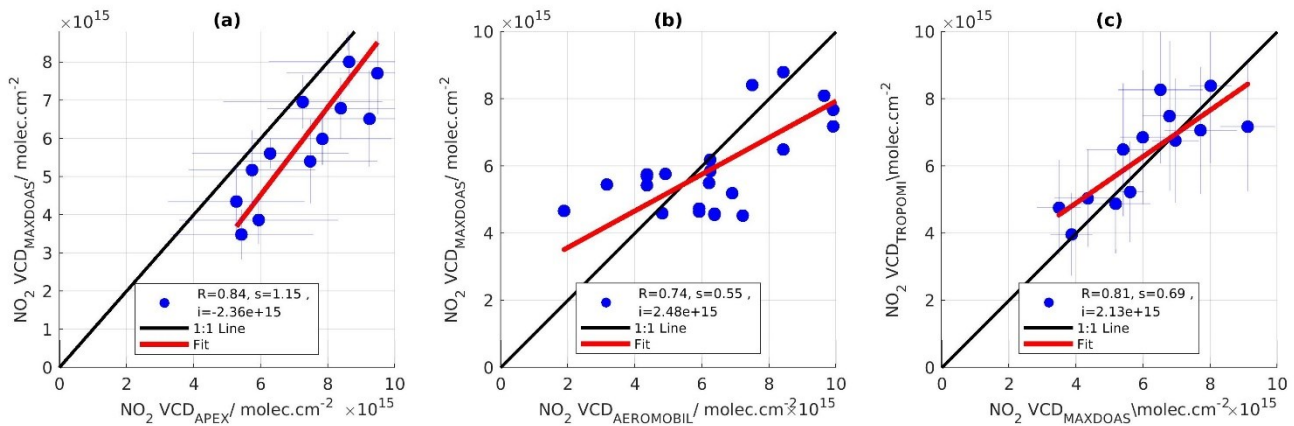
Figure 20. Scatter plot between (a) the tropospheric NO₂ columns derived by airborne measurements (APEX) and the MAX-DOAS observations, (b) the tropospheric NO₂ columns derived by car mobile-DOAS measurements (AEROMOBIL), and the MAX-DOAS observations and (c) the tropospheric NO₂ columns derived by MAX-DOAS observations and the TROPOMI tropospheric NO₂ columns over Brussels on 28th of June 2019.

 5.3 Comparison of MAX-DOAS horizontal NO₂ distribution versus TROPOMI observations

To compare the TROPOMI and MAX-DOAS tropospheric NO₂ columns, the following 5-step approach is used, similarly as in Section 5.2:

1. Only MAX-DOAS horizontal profiles of tropospheric NO₂ VCDs retrieved around (±1 hour) TROPOMI overpass time are selected.

2. The time-coincident MAX-DOAS tropospheric NO_2 VCD horizontal grids from all the azimuthal directions are spatially averaged (i.e. one MAX-DOAS mean NO_2 VCD value per pixel) within the overlapping TROPOMI pixels.

3. The MAX-DOAS segments are weighted by their relative length inside each TROPOMI pixel.

4. The horizontal profiles of MAX-DOAS NO_2 columns have a horizontal sampling of 0.5 km in every azimuthal direction. The coverage percentage is estimated as the ratio of the area covered by MAX-DOAS (i.e., number of coincident MAX-DOAS NO_2 VCDs considering that every MAX-DOAS horizontal grid has a spatial resolution of 0.5 x 0.5 km^2) inside each TROPOMI pixel to the total number of MAX-DOAS NO_2 VCDs that could fill-in the TROPOMI pixel.

5. TROPOMI and MAX-DOAS tropospheric NO_2 columns are compared, and the seasonally-averaged maps of those VCDs on the area covered by the TROPOMI pixels are created. To generate these maps, the ensemble of TROPOMI pixels recorded on 28 June 2019 is chosen as reference and TROPOMI pixels that coincide with this reference grid are averaged. The daily horizontal profiles of MAX-DOAS NO_2 columns are averaged on the daily TROPOMI grids and then, the reference grid is used to create the seasonally-averaged MAX-DOAS maps.

The seasonally and annually-averaged maps of TROPOMI and MAX-DOAS NO_2 VCDs are presented in Fig. 21 and Fig. 22. Only pixels including at least 20 comparison days are taken into account in the analysis. It is found that the locations of the NO_2 peaks and dips show a reasonably high degree of similarity between TROPOMI and MAX-DOAS during all seasons, except summer. The NO_2 peaks appear mainly above Brussels city center, the Drogenbos power plant (W direction) and the NW part of the Ring road, which are the main known emission sources, as mentioned earlier. These maps also indicate that the tropospheric NO_2 column over the Brussels area has a clear seasonal cycle, with a maximum during winter.

Figure 22c shows the annual relative biases (e.g., 100 x (TROPOMI – MAX-DOAS)/MAX-DOAS) per pixel. It is found that positive biases (i.e. TROPOMI larger than MAX-DOAS) are observed mainly in the pixels located away from the measurement site during all seasons, while negative biases are found close to the measurement site and in the Brussels city center.

The seasonal correlation plots for April 2018-February 2020 are displayed in Fig. 23. When all pixels are included, without any TROPOMI pixels coverage percentage filtering on MAX-DOAS data, the highest correlation is found during spring (R=0.70), while lower correlations are reported in autumn, summer, and winter, with correlation coefficient values of 0.60, 0.58, and 0.56, respectively. It should be noted that during spring (2018 and 2019), the number of comparison points is smaller than for the other seasons, because TROPOMI data start from end of April 2018. During spring, the slope value is equal to 1.06, while during winter, summer, and autumn, the slope values are smaller (0.78, 0.53, and 0.78, respectively). Similar findings have been reported in several studies (Verhoelst et al., 2021; Tack et al., 2021; Judd et al., 2020; Dimitropoulou et al., 2020; Ialongo et al., 2019). When seasonally-averaged TROPOMI and MAX-DOAS pixels (the pixels shown in Fig. 21) are compared one-by-one (see seasonal (SEAS) in Fig. 23), both correlation coefficient (R in the range of 0.42-0.92) and slope values (s in the range of 0.44-1.90) improve considerably for spring and autumn.

825 In a second step, the impact of the spatial sampling is investigated. Generally, a varying number of MAX-DOAS NO_2 columns cover each TROPOMI pixel. The coverage percentage is estimated as the ratio of the covered area by MAX-DOAS (i.e., number of coincident MAX-DOAS NO_2 VCDs) inside each TROPOMI pixel to the total number of MAX-DOAS NO_2 VCDs that could fill-in the TROPOMI pixel. When selecting only TROPOMI pixels covered by at least a given percentage of MAX-DOAS grids (10% and 20%), it is found that the correlation between both datasets improves for all seasons, except summer

830 for a coverage equal and greater than 20%. The most significant improvement is observed during spring. The correlation coefficient value is equal to 0.82 (instead of 0.70) when taking into account TROPOMI pixels covered more than 20% by MAX-DOAS retrievals. Despite the better agreement in terms of correlation coefficient, TROPOMI columns are still 30 % lower than MAX-DOAS measurements, in line with previously published studies.

835 The seasonal regression analysis parameters between TROPOMI and dual-scan MAX-DOAS measurements derived in the present study are compared to the same parameters presented in Dimitropoulou et al. (2020), see Table 4. Both studies make use of the dual-scan MAX-DOAS instrument in Uccle. In addition to the different approach (i.e., the retrieval of NO_2 horizontal profiles), in the present study, almost two years of measurements are used, while in Dimitropoulou et al. (2020), only one year is exploited for the TROPOMI validation. In Table 4, for the present study, only one year of measurements are used to have a

840 comparable time coverage for both studies. As presented in Table 4, here, the largest slope value is found in spring, while in Dimitropoulou et al. (2020), in winter. The season in which the highest correlation coefficient is obtained differs between both studies (here, in spring, in autumn in Dimitropoulou et al. (2020)). The main advantage of the new mapping MAX-DOAS technique is the larger number of comparison points between TROPOMI and MAX-DOAS leading to significantly more reliable statistics. In the present study, the deviation of the comparison points from the fitted regression line is increased mainly

845 because of the uncertainties in the horizontal inversion approach. The scatter increase is reflected in the correlation coefficient values, which are smaller for all seasons, except winter. Regarding the slope value, it is larger in spring and summer, and is smaller in autumn and winter.

850
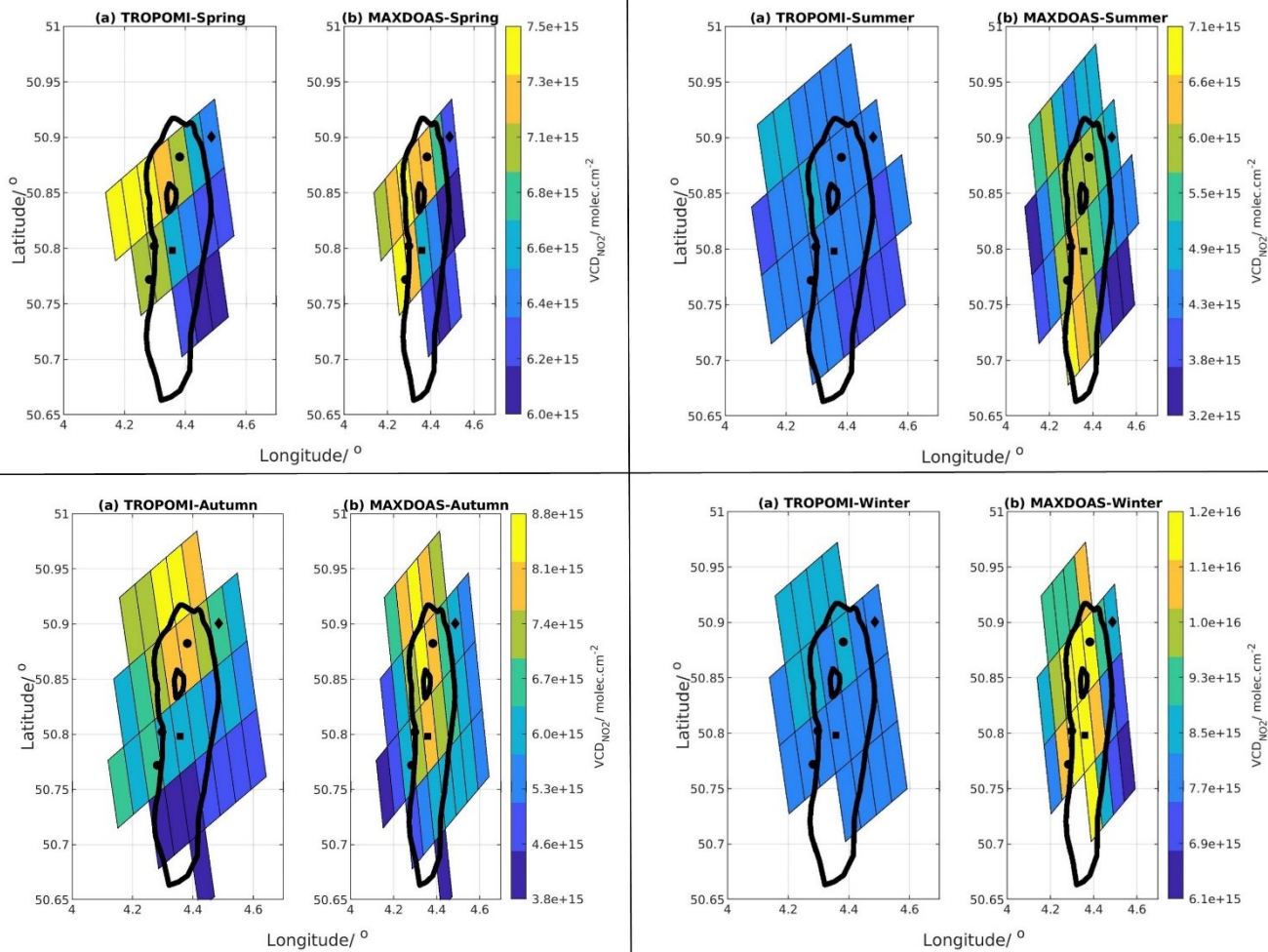
855

Figure 21. Seasonal tropospheric NO₂ VCD grids (TROPOMI grids) as retrieved over Brussels by the TROPOMI and MAX-DOAS instruments. The black square shows the MAX-DOAS position, the black polygon the National Airport, the black dots the NO₂ hotspots, and the black line represents the Brussels Ring motorway.

860
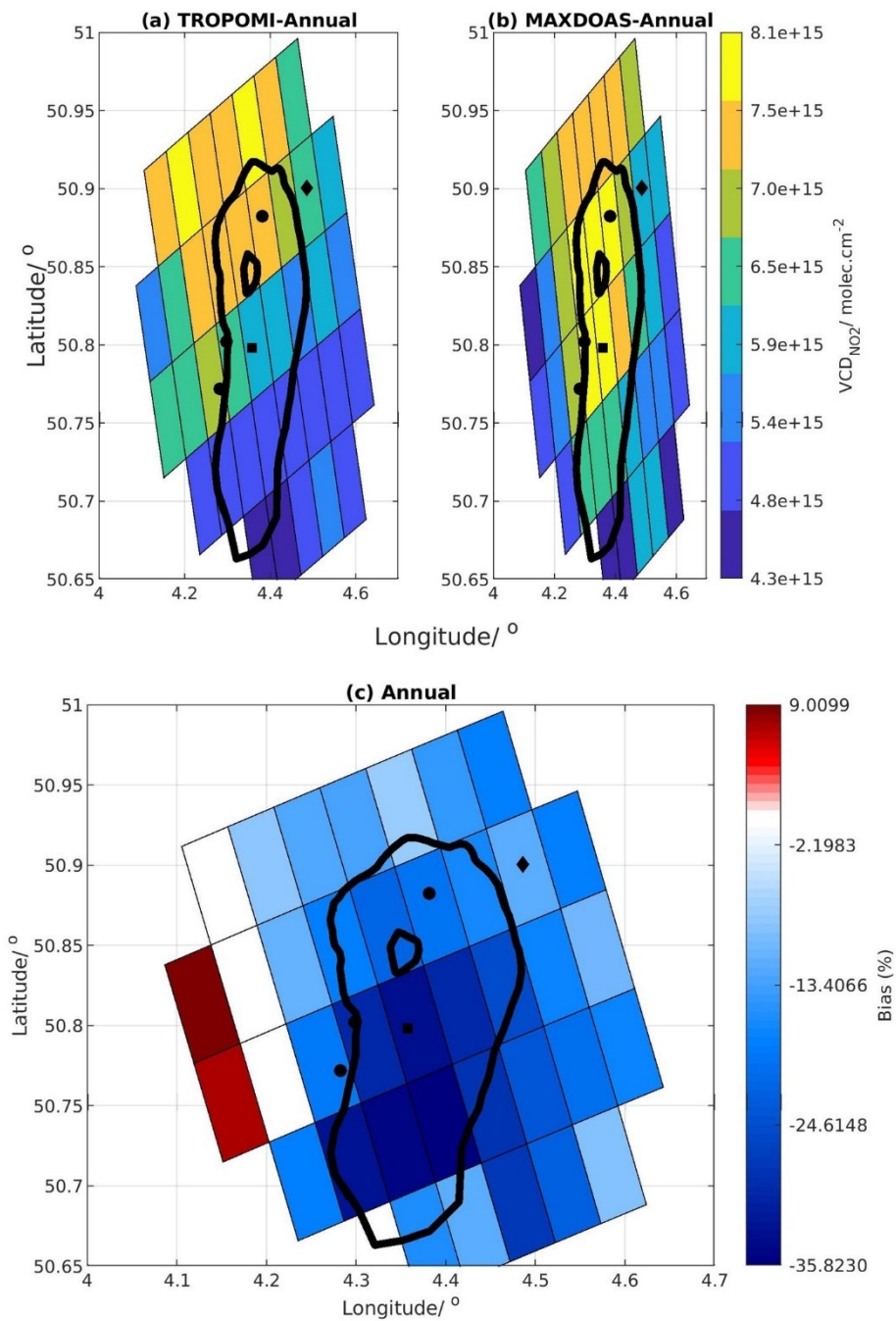
Figure 22. Annual (e.g., based over the two years of observations) tropospheric NO₂ VCD grids (TROPOMI grids) as retrieved over Brussels by the (a) TROPOMI and (b) MAX-DOAS instruments. (c) Annual bias between tropospheric NO₂ VCD as observed by TROPOMI and MAX-DOAS instruments (the negative values are shown with blue color,

865   **zero with white, and positive values with red). The black square shows the MAX-DOAS instrument location, the black polygon the National Airport, the black dots the NO$_2$ hotspots, and the black line represents the Brussels Ring road.**

870

875

880
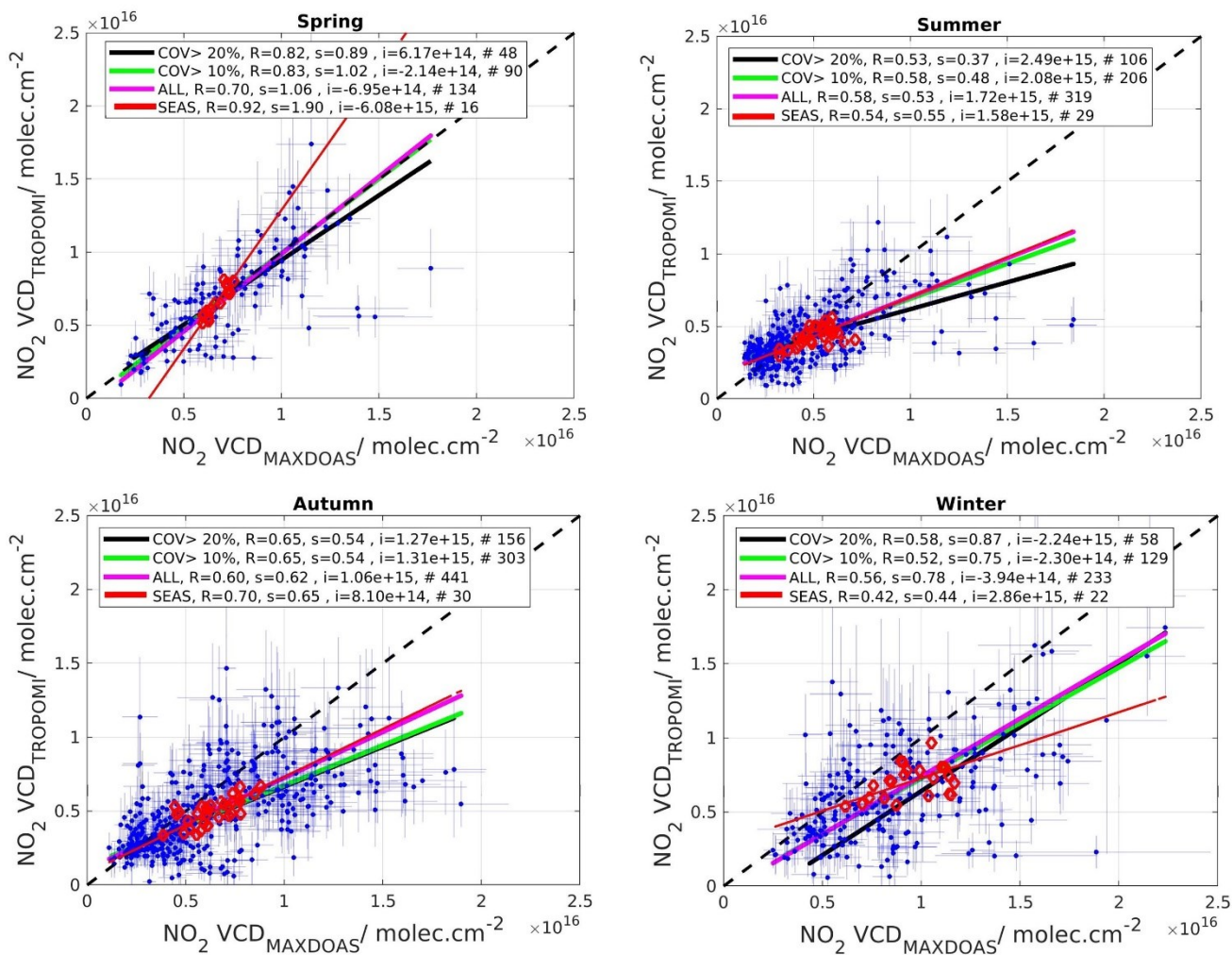
Figure 23. Seasonal scatter plots of tropospheric NO₂ columns derived from the dual-scan MAX-DOAS and TROPOMI measurements over Brussels. Magenta line: Regression analysis results when all the MAX-DOAS and TROPOMI pixels are included in the comparison. Green and black lines: Regression analysis results when TROPOMI pixels covered (i.e., COV) by more than 10 and 20 % of the horizontal profiles of MAX-DOAS NO₂ columns are included in the comparison. Red line: Seasonal average analysis generated by the pixels in Fig. 21.

Table 4. Summary of the regression analysis parameters (e.g., correlation coefficient (R) and slope (s)) and the number
 of data points (N) derived in the present study during only one year of observations (i.e., number of pixels) and in Dimitropoulou et al. (2020). Please note that R (seasonal) and s (seasonal) corresponds to SEAS in Figure 23.

Season	Spring	Summer	Autumn	Winter
R	0.66	0.60	0.57	0.62
R (seasonal)	0.93	0.88	0.46	0.75
R (Dimitropoulou et al., 2020)	0.69	0.77	0.85	0.60
s	0.90	0.76	0.56	0.60
s (seasonal)	0.94	0.87	0.74	0.70
s (Dimitropoulou et al., 2020)	0.47	0.58	0.61	0.81
N	139	247	106	92
N (Dimitropoulou et al., 2020)	16	58	36	13

6 Conclusions

Two years (March 2018 to February 2020) of dual-scan MAX-DOAS measurements in Uccle (urban background site located in the south of the Brussels-Capital Region) were used to develop a new strategy for the retrieval of near-surface NO_2 concentrations and aerosol extinction horizontal profiles. A full dual-scan measurement is composed of one vertical scan at a
930 fixed azimuthal direction pointing towards the city center and horizontal scans in ten azimuthal directions at a fixed low elevation angle (2°).

The first step of this new retrieval strategy is to analyze measured radiance spectra in six different fitting windows. This provides O_4 and NO_2 dSCDs at the following six wavelengths: 343 nm, 360 nm, 380 nm, 447 nm, 477 nm and 530 nm. Then, information about the vertical extent of NO_2 in the troposphere (MLH_{NO2}) is derived from profile retrievals in the main
935 azimuthal direction performed using the OEM-based MMF algorithm. In the third step, a new parameterization technique is applied, with MLH_{NO2}, measured O_4 dSCDs, and measurement geometry being used as input parameters to retrieve the horizontal sensitivity of NO_2 and, consequently, the NO_2 near-surface concentrations and VCDs, near-surface aerosol extinction and AODs in all the azimuthal directions for the six different wavelengths. Compared to the method presented in Dimitropoulou et al., (2020), the new retrieval method offers the possibility of the direct determination of L_{NO2}, and near-
940 surface aerosol extinction based on the measured O_4 dSCDs.

The retrieved dual-scan NO_2 near-surface concentrations and VCDs are verified via comparisons to the MMF NO_2 vertical profiles derived in the main azimuthal directions and in three additional azimuthal directions. A good overall agreement is found for the two comparisons during the two years of measurements.

The dependence of the horizontal sensitivity on the wavelength is then used to develop a new OEM-based horizontal
945 distribution inversion approach. Considering a horizontal box model, horizontal NO_2 and aerosol extinction profiles are retrieved in an output horizontal grid of 500m thickness starting from the instrument to each of the measurement maximum horizontal representative distance.

The daily variability of NO_2 horizontal profiles in all the azimuthal directions provides information about the location of the NO_2 hotspots in the Brussels-Capital Region and how the plumes are transported. Similarly, the NO_2 horizontal profiles'
950 seasonal variability over March 2018-February 2020 reveals that the NO_2 hotspots are mainly found above the Brussels city-center, the Drogenbos power plant and the NW part of the Ring road during all seasons.

On 28 June 2019, airborne measurements (APEX) of NO_2 were performed over Brussels. The MAX-DOAS NO_2 VCD horizontal profiles are compared to APEX, mobile car-DOAS (i.e., AEROMOBIL), and TROPOMI measurements, and a good overall agreement is found between the different data sets for this day.

955 In the last part of the study, MAX-DOAS retrievals are compared to TROPOMI tropospheric NO_2 observations over the March 2018- February 2020 period. The comparison of seasonal maps shows a good overall agreement between both datasets as to

the NO$_2$ horizontal distribution over the Brussels area. During all seasons, except summer, this agreement improves systematically when only TROPOMI pixels covered by a minimum of 20% of MAX-DOAS grid cells are compared, showing the benefit of ground-based measurements at high horizontal resolution for the validation of high-resolution space-borne air-quality measurements. Results also show that during all seasons, TROPOMI underestimates the MAX-DOAS tropospheric NO$_2$ columns.

Overall, our investigation about the spatial sampling lead to the following three important findings:

1. The dual-scan multi-wavelength approach allows a better identification of the main emissions sources in urban regions, in agreement with the spatial allocation of the main emission sources observed by APEX and TROPOMI.

2. The characterization of the NO$_2$ concentration horizontal field using the dual scan multi-wavelength approach results in obtaining larger slope values between TROPOMI and MAX-DOAS observations. The high spatial resolution of TROPOMI requires ground-based measurement that can provide information about the horizontal distribution of tropospheric NO$_2$ columns in urban regions.

3. Even for a better spatial sampling between TROPOMI and ground-based observations, TROPOMI still underestimates the ground-based measurements (see Fig. 22). Therefore, this is an additional indication that this underestimation is caused by other factors.

The role of the a priori NO$_2$ profile shape in the TROPOMI retrievals was investigated and TROPOMI tropospheric NO$_2$ columns are recalculated with the MAX-DOAS vertical profiles. We show that the knowledge of the NO$_2$ horizontal distribution derived by the MAX-DOAS measurements combined with a more adequate a priori profile in TROPOMI retrievals leads to a much better agreement between satellite and ground-based data.

To conclude, our study presents a new horizontal distribution inversion approach for NO$_2$ and aerosols developed by using dual-scan multi-wavelength MAX-DOAS measurements over an urban area. This approach provides a better characterization of the horizontal distribution of an important urban pollutant, NO$_2$, which leads to an improved agreement between satellite and MAX-DOAS measurements in moderate to highly polluted conditions. Based on our study, further modifications of the measurement mode aiming at a better sampling of the vertical and horizontal NO$_2$ distribution could be implemented and investigated. For instance, performing vertical scans in several azimuthal directions throughout the day and/or horizontal scans in more than ten azimuthal directions could further improve our knowledge about the tropospheric NO$_2$ spatial variability in urban regions, and therefore the satellite validation results in those conditions.

Data availability. The datasets generated and analyzed in the present work are available from the corresponding author on request.

990 *Author contributions.* ED undertook the development and validation of the dual-scan multi-wavelength MAX-DOAS retrieval strategy in Uccle, exploited the MAX-DOAS retrievals during two year, performed the validation of the TROPOMI tropospheric NO2 columns, and wrote the paper. FH supported and guided ED in the development of the dual-scan multi-wavelength MAX-DOAS retrieval strategy, provided general guidelines, and revised and edited the paper. MMF provided the MMF inversion algorithm and the RTM as well as supporting and guiding ED in the new OEM-based horizontal profile

995 retrieval. FT provided the airborne APEX dataset and contributed to scientific discussions. GP provided the dataset of the TROPOMI tropospheric NO2 columns and supported ED in the TROPOMI validation approaches. AM provided the AEROMOBIL dataset and contributed to scientific discussions. CF and CH provided technical and software support for the MAX-DOAS instrument in Uccle. CF developed the QDOAS software and guided ED in the DOAS analysis. FF provided the RIO model dataset. MVR supervised the present work, provided general guidelines and valuable comments during the whole

1000 process of the paper preparation, and revised and edited the paper. All authors reviewed, discussed and commented on the paper.

Competing interests. I declare that I or my co-authors have competing interests as follows: Michel Van Roozendael is associate editor of AMT.

1005

References

1010 Aliwell, S.R., Van Roozendael, M., Johnston, P.V., Richter, A., Wagner, T., Arlander, D.W., Burrows, J.P., Fish, D.J., Jones, R.L., Tørnkvist, K.K. and Lambert, J.C., 2002. Analysis for BrO in zenith-sky spectra: An intercomparison exercise for analysis improvement. *Journal of Geophysical Research: Atmospheres*, *107*(D14), pp.ACH-10.

Barret, B., De Maziere, M., and Demoulin, P.: Retrieval and ` characterisation of ozone profiles from solar infrared spectra at the Jungfraujoch, J. Geophys. Res., 107 (D24), 4788, doi:10.1029/2001JD001298, 2002.

1015 Beirle, S., Dörner, S., Donner, S., Remmers, J., Wang, Y., and Wagner, T.: The Mainz profile algorithm (MAPA), Atmos. Meas. Tech., 12, 1785–1806, https://doi.org/10.5194/amt-12- 1785-2019, 2019.

Beirle, S., Platt, U., Wenig, M., and Wagner, T.: Weekly cycle of NO_2 by GOME measurements: a signature of anthropogenic sources, Atmos. Chem. Phys., 3, 2225–2232, https://doi.org/10.5194/acp-3-2225-2003, 2003.

Bösch, T., Rozanov, V., Richter, A., Peters, E., Rozanov, A., Wittrock, F., Merlaud, A., Lampel, J., Schmitt, S., de Haij, M.,

1020 Berkhout, S., Henzing, B., Apituley, A., den Hoed, M., Vonk, J., Tiefengraber, M., Müller, M., and Burrows, J. P.: BOREAS – a new MAX-DOAS profile retrieval algorithm for aerosols and trace gases, Atmos. Meas. Tech., 11, 6833–6859, https://doi.org/10.5194/amt-11-6833-2018, 2018.

Burrows, J. P., Weber, M., Buchwitz, M., Rosanov, V. V., Ladstatter, A., Weissenmayer, A., Richter, A., DeBeek, R., Hoogen, R., Bramstedt, K., and Eichmann, K. U.: The Global Ozone Monitoring Experiment (GOME): Mission concept and first scientific results, J. Atmos. Sci., 56, 151–175, 1999.

Chance, K. V. and Spurr, R. J. D.: Ring effect studies: Rayleigh scattering, including molecular parameters for rotational Raman scattering, and the Fraunhofer spectrum, Appl. Optics, 36, 5224– 5230, doi:10.1364/AO.36.005224, 1997.

Chan, K. L., Wiegner, M., van Geffen, J., De Smedt, I., Alberti, C., Cheng, Z., Ye, S., and Wenig, M.: MAX-DOAS measurements of tropospheric NO_2 and HCHO in Munich and the comparison to OMI and TROPOMI satellite observations, Atmos. Meas. Tech., 13, 4499–4520, https://doi.org/10.5194/amt-13-4499-2020, 2020.

Chen, T. M., Kuschner, W. G., Gokhale, J., & Shofer, S. (2007). Outdoor air pollution: nitrogen dioxide, sulfur dioxide, and carbon monoxide health effects. *The American journal of the medical sciences*, *333*(4), 249-256.

Clémer, K., Van Roozendael, M., Fayt, C., Hendrick, F., Hermans, C., Pinardi, G., Spurr, R., Wang, P., and De Mazière, M.: Multiple wavelength retrieval of tropospheric aerosol optical properties from MAXDOAS measurements in Beijing, Atmos. Meas. Tech., 3, 863–878, https://doi.org/10.5194/amt-3-863-2010, 2010.

Compernolle, S., Argyrouli, A., Lutz, R., Sneep, M., Lambert, J.-C., Fjæraa, A. M., Hubert, D., Keppens, A., Loyola, D., O'Connor, E., Romahn, F., Stammes, P., Verhoelst, T., and Wang, P.: Validation of the Sentinel-5 Precursor TROPOMI cloud data with Cloudnet, Aura OMI O_2–O_2, MODIS, and Suomi-NPP VIIRS, Atmos. Meas. Tech., 14, 2451–2476, https://doi.org/10.5194/amt-14-2451-2021, 2021.

Dimitropoulou, E., Hendrick, F., Pinardi, G., Friedrich, M. M., Merlaud, A., Tack, F., De Longueville, H., Fayt, C., Hermans, C., Laffineur, Q., Fierens, F., and Van Roozendael, M.: Validation of TROPOMI tropospheric NO2 columns using dual scan multi-axis differential optical absorption spectroscopy (MAX-DOAS) measurements in Uccle, Brussels, Atmos. Meas. Tech., 13, 5165–5191, https://doi.org/10.5194/amt-13-5165-2020, 2020.

Douros, J., Eskes, H., van Geffen, J., Boersma, F., Compernolle, S., Pinardi, G., Blechschmidt, A-M., Peuch, V-H., Colette, A., and Veefkind P.: Comparing Sentinel-5P TROPOMI NO_2 column observations with the CAMS-regional air quality ensemble, in preparation.

Eskes, H.J. and Eichmann, K.U.: *S5P MPC Product Readme Nitrogen Dioxide*. Report S5P-MPC-KNMI PRF-NO2, version 1.4, 6 August 2019, ESA, available at: http://www. tropomi. eu/documents/prf/, 17 March, 2020.

Fayt, C., De Smedt, I., Letocart, V., Merlaud, A., Pinardi, G., and Van Roozendael, M.: QDOAS Software user manual, http://uv-vis.aeronomie.be/software/QDOAS/index.php, 2011.

Fleischmann, O. C., Hartmann, M., Burrows, J. P., and Orphal, J.: New ultraviolet absorption cross-sections of BrO at atmospheric temperatures measured by time-windowing Fourier transform spectroscopy, J. Photoch. Photobio. A, 168, 117–132, 2004.

Friedrich, M. M., Rivera, C., Stremme, W., Ojeda, Z., Arellano, J., Bezanilla, A., García-Reynoso, J. A., and Grutter, M.: NO_2 vertical profiles and column densities from MAX-DOAS measurements in Mexico City, Atmos. Meas. Tech., 12, 2545–2565, https://doi.org/10.5194/amt-12-2545-2019, 2019.

Hendrick, F., Müller, J.-F., Clémer, K., Wang, P., De Mazière, M., Fayt, C., Gielen, C., Hermans, C., Ma, J. Z., Pinardi, G., Stavrakou, T., Vlemmix, T., and Van Roozendael, M.: Four years of ground-based MAX-DOAS observations of HONO and NO2 in the Beijing area, Atmos. Chem. Phys., 14, 765–781, https://doi.org/10.5194/acp-14-765-2014, 2014.

1060 Hönninger, G., von Friedeburg, C., and Platt, U.: Multi axis differential optical absorption spectroscopy (MAX-DOAS), Atmos. Chem. Phys., 4, 231–254, doi:10.5194/acp-4-231-2004, 2004.

Hooyberghs, J., Mensink, C., Dumont, G. and Fierens, F., 2006. Spatial interpolation of ambient ozone concentrations from sparse monitoring points in Belgium. *Journal of Environmental Monitoring*, *8*(11), pp.1129-1135.

Ialongo, I., Virta, H., Eskes, H., Hovila, J., and Douros, J.: Comparison of TROPOMI/Sentinel 5 Precursor NO$_2$ observations
1065 with ground-based measurements in Helsinki, Atmos. Meas. Tech. Discuss., https://doi.org/10.5194/amt-2019-329, in review, 2019.

Irie, H., Takashima, H., Kanaya, Y., Boersma, K. F., Gast, L., Wittrock, F., Brunner, D., Zhou, Y., and Van Roozendael, M.: Eight-component retrievals from ground-based MAXDOAS observations, Atmos. Meas. Tech., 4, 1027–1044, https://doi.org/10.5194/amt-4-1027-2011, 2011.

1070 Irie, H., Boersma, K. F., Kanaya, Y., Takashima, H., Pan, X., and Wang, Z. F.: Quantitative bias estimates for tropospheric NO2 columns retrieved from SCIAMACHY, OMI, and GOME-2 using a common standard for East Asia, Atmos. Meas. Tech., 5, 2403–2411, https://doi.org/10.5194/amt-5-2403-2012, 2012.

Janssen, S., Dumont, G., Fierens, F. and Mensink, C., 2008. Spatial interpolation of air pollution measurements using CORINE land cover data. *Atmospheric Environment*, *42*(20), pp.4884-4903.

1075 Judd, L. M., Al-Saadi, J. A., Szykman, J. J., Valin, L. C., Janz, S. J., Kowalewski, M. G., Eskes, H. J., Veefkind, J. P., Cede, A., Mueller, M., Gebetsberger, M., Swap, R., Pierce, R. B., Nowlan, C. R., Abad, G. G., Nehrir, A., and Williams, D.: Evaluating Sentinel-5P TROPOMI tropospheric NO2 column densities with airborne and Pandora spectrometers near New York City and Long Island Sound, Atmos. Meas. Tech., 13, 6113–6140, https://doi.org/10.5194/amt-13-6113-2020, 2020.

1080 Khomenko, S., Cirach, M., Pereira-Barboza, E., Mueller, N., Barrera-Gómez, J., Rojas-Rueda, D., de Hoogh, K., Hoek, G. and Nieuwenhuijsen, M., 2021. Premature mortality due to air pollution in European cities: a health impact assessment. *The Lancet Planetary Health*, *5*(3), pp.e121-e134.

Klimont, Z., Kupiainen, K., Heyes, C., Purohit, P., Cofala, J., Rafaj, P., Borken-Kleefeld, J., and Schöpp, W.: Global anthropogenic emissions of particulate matter including black carbon, Atmos. Chem. Phys., 17, 8681–8723,
1085 https://doi.org/10.5194/acp-17-8681-2017, 2017.

Kreher, K., Van Roozendael, M., Hendrick, F., Apituley, A., Dimitropoulou, E., Frieß, U., Richter, A., Wagner, T., Abuhassan, N., Ang, L., Anguas, M., Bais, A., Benavent, N., Bösch, T., Bognar, K., Borovski, A., Bruchkouski, I., Cede, A., Chan, K. L., Donner, S., Drosoglou, T., Fayt, C., Finkenzeller, H., Garcia-Nieto, D., Gielen, C., Gómez-Martín, L., Hao, N., Herman, J. R., Hermans, C., Hoque, S., Irie, H., Jin, J., Johnston, P., Khayyam Butt, J., Khokhar, F., Koenig, T. K.,
1090 Kuhn, J., Kumar, V., Lampel, J., Liu, C., Ma, J., Merlaud, A., Mishra, A. K., Müller, M., Navarro-Comas, M., Ostendorf,

M., Pazmino, A., Peters, E., Pinardi, G., Pinharanda, M., Piters, A., Platt, U., Postylyakov, O., Prados-Roman, C., Puentedura, O., Querel, R., Saiz-Lopez, A., Schönhardt, A., Schreier, S. F., Seyler, A., Sinha, V., Spinei, E., Strong, K., Tack, F., Tian, X., Tiefengraber, M., Tirpitz, J.-L., van Gent, J., Volkamer, R., Vrekoussis, M., Wang, S., Wang, Z., Wenig, M., Wittrock, F., Xie, P. H., Xu, J., Yela, M., Zhang, C., and Zhao, X.: Intercomparison of NO_2, O_4, O_3 and HCHO slant column measurements by MAX-DOAS and zenith-sky UV-Visible spectrometers during the CINDI-2 campaign, Atmos. Meas. Tech. Discuss., https://doi.org/10.5194/amt-2019-157, in review, 2019.

Kurucz, R.L., Furenlid, I., Brault, J., and Testerman, L.: Solar flux atlas from 296 to 1300 nm, National Solar Observatory, Sunspot, New Mexico, U.S.A., 1984.

Meller, R. and Moortgat, G. K.: Temperature dependence of the absorption cross sections of formaldehyde between 223 and 323K in the wavelength range 225–375nm, J. Geophys. Res., 105, 7089–7101, 2000.

Merlaud, A., Van Roozendael, M., Theys, N., Fayt, C., Hermans, C., Quennehen, B., Schwarzenboeck, A., Ancellet, G., Pommier, M., Pelon, J., Burkhart, J., Stohl, A., and De Mazière, M.: Airborne DOAS measurements in Arctic: vertical distributions of aerosol extinction coefficient and NO2 concentration, Atmos. Chem. Phys., 11, 9219–9236, https://doi.org/10.5194/acp11-9219-2011, 2011.

Merlaud, A.: Development and use of compact instruments for tropospheric investigations based on optical spectroscopy from mobile platforms, Presses Universitaires de Louvain, 2013.

Pinardi, G., Hendrick, F., Clémer, K., Lambert, J. C., Bai, J., and Van Roozendael, M.: On the use of the MAX-DOAS technique for the validation of tropospheric NO2 column measurements from satellite, Proc. Eumetsat Conf., ISBN 978-92-9110-082-8, 2008.

Puķīte, J., Kühl, S., Deutschmann, T., Platt, U., and Wagner, T.: Extending differential optical absorption spectroscopy for limb measurements in the UV, Atmos. Meas. Tech., 3, 631–653, https://doi.org/10.5194/amt-3-631-2010, 2010.

Quaas, Johannes, Olivier Boucher, Nicolas Bellouin, and Stefan Kinne. "Satellite-based estimate of the direct and indirect aerosol climate forcing." *Journal of Geophysical Research: Atmospheres* 113, no. D5 (2008).

Rodgers, C. D.: Inverse Methods for Atmospheric Sounding, Theory and Practice, World Scientific Publishing, Singapore – NewJersey – London – Hong Kong, 2000.

Rothman, L.S., Gordon, I.E., Babikov, Y., Barbe, A., Benner, D.C., Bernath, P.F., Birk, M., Bizzocchi, L., Boudon, V., Brown, L.R. and Campargue, A., 2013. The HITRAN2012 molecular spectroscopic database. *Journal of Quantitative Spectroscopy and Radiative Transfer*, *130*, pp.4-50.Seinfeld, J. H. and Pandis, S. N.: Atmospheric Chemistry and Physics: From Air Pollution to Climate Change, John Wiley & Sons, Inc., 1998.

Schreier, S. F., Bösch, T., Richter, A., Lange, K., Revesz, M., Weihs, P., Vrekoussis, M., and Lotteraner, C.: Evaluation of UV–visible MAX-DOAS aerosol profiling products by comparison with ceilometer, sun photometer, and in situ observations in Vienna, Austria, Atmos. Meas. Tech., 14, 5299–5318, https://doi.org/10.5194/amt-14-5299-2021, 2021.

Serdyuchenko, A., Gorshelev, V., Weber, M., Chehade, W., and Burrows, J. P.: High spectral resolution ozone absorption crosssections – Part 2: Temperature dependence, Atmos. Meas. Tech., 7, 625–636, doi:10.5194/amt-7-625-2014, 2014.

Sinreich, R., Volkamer, R., Filsinger, F., Frieß, U., Kern, C., Platt, U., Sebastián, O., and Wagner, T.: MAX-DOAS detection of glyoxal during ICARTT 2004, Atmos. Chem. Phys., 7, 1293–1303, https://doi.org/10.5194/acp-7-1293-2007, 2007.

Sinreich, R., Merten, A., Molina, L., and Volkamer, R.: Parameterizing radiative transfer to convert MAX-DOAS dSCDs into near-surface box-averaged mixing ratios, Atmos. Meas. Tech., 6, 1521–1532, doi:10.5194/amt-6-1521-2013, 2013.

Spurr, R. J.: VLIDORT: A linearized pseudo-spherical vector discrete ordinate radiative transfer code for forward model and retrieval studies in multilayer multiple scattering media, J. Quant. Spectrosc. Ra., 102, 316–342, 2006.

Tack, F., Merlaud, A., Iordache, M.-D., Danckaert, T., Yu, H., Fayt, C., Meuleman, K., Deutsch, F., Fierens, F., and Van Roozendael, M.: High-resolution mapping of the NO_2 spatial distribution over Belgian urban areas based on airborne APEX remote sensing, Atmos. Meas. Tech., 10, 1665–1688, https://doi.org/10.5194/amt-10-1665-2017, 2017.

Tack, F., Merlaud, A., Meier, A. C., Vlemmix, T., Ruhtz, T., Iordache, M.-D., Ge, X., van der Wal, L., Schuettemeyer, D., Ardelean, M., Calcan, A., Constantin, D., Schönhardt, A., Meuleman, K., Richter, A., and Van Roozendael, M.: Intercomparison of four airborne imaging DOAS systems for tropospheric NO_2 mapping – the AROMAPEX campaign, Atmos. Meas. Tech., 12, 211–236, https://doi.org/10.5194/amt-12-211-2019, 2019.

Tack, F., Merlaud, A., Iordache, M.-D., Pinardi, G., Dimitropoulou, E., Eskes, H., Bomans, B., Veefkind, P., and Van Roozendael, M.: Assessment of the TROPOMI tropospheric NO_2 product based on airborne APEX observations, Atmos. Meas. Tech., 14, 615–646, https://doi.org/10.5194/amt-14-615-2021, 2021.

Thalman, R. and Volkamer, R.: Temperature dependent absorption cross-sections of O2-O2 collision pairs between 340 and 630nm and at atmospherically relevant pressure, Phys. Chem. Chem. Phys., 15, 15371–15381, doi:10.1039/C3CP50968K, 2013.

Tirpitz, J.-L., Frieß, U., Hendrick, F., Alberti, C., Allaart, M., Apituley, A., Bais, A., Beirle, S., Berkhout, S., Bognar, K., Bösch, T., Bruchkouski, I., Cede, A., Chan, K. L., den Hoed, M., Donner, S., Drosoglou, T., Fayt, C., Friedrich, M. M., Frumau, A., Gast, L., Gielen, C., Gomez-Martín, L., Hao, N., Hensen, A., Henzing, B., Hermans, C., Jin, J., Kreher, K., Kuhn, J., Lampel, J., Li, A., Liu, C., Liu, H., Ma, J., Merlaud, A., Peters, E., Pinardi, G., Piters, A., Platt, U., Puentedura, O., Richter, A., Schmitt, S., Spinei, E., Stein Zweers, D., Strong, K., Swart, D., Tack, F., Tiefengraber, M., van der Hoff, R., van Roozendael, M., Vlemmix, T., Vonk, J., Wagner, T., Wang, Y., Wang, Z., Wenig, M., Wiegner, M., Wittrock, F., Xie, P., Xing, C., Xu, J., Yela, M., Zhang, C., and Zhao, X.: Intercomparison of MAX-DOAS vertical profile retrieval algorithms: studies on field data from the CINDI-2 campaign, Atmos. Meas. Tech., 14, 1–35, https://doi.org/10.5194/amt-14-1-2021, 2021.

van Geffen, J. H. G. M., Eskes, H. J., Boersma, K. F. and Veefkind, J. P.: TROPOMI ATBD of the total and tropospheric NO_2 data products, Report S5P-KNMI-L2-0005-RP, version 2.2.0, released 16 June 2021, KNMI, De Bilt, The Netherlands, http://www.tropomi.eu/ data-products/nitrogen-dioxide/, 2021a.

van Geffen, J., Eskes, H., Compernolle, S., Pinardi, G., Verhoelst, T., Lambert, J.-C., Sneep, M., ter Linden, M., Ludewig, A., Boersma, K. F., and Veefkind, J. P.: Sentinel-5P TROPOMI NO_2 retrieval: impact of version v2.2 improvements and comparisons with OMI and ground-based data, Atmos. Meas. Tech. Discuss. [preprint], https://doi.org/10.5194/amt-

2021-329, in review, 2021b.Vandaele, A., Hermans, C., Simon, P., Carleer, M., Colin, R., Fally, S., Mérienne, M., Jenouvrier, A., and Coquart, B.: Measurements of the NO2 absorption cross-section from 42000cm−1 to 10000cm−1 (238–1000nm) at 220K and 294K, J. Quant. Spectrosc. Ra., 59, 171–184, 1998.

Veefkind, J. P., Boersma, K. F., Wang, J., Kurosu, T. P., Krotkov, N., Chance, K., and Levelt, P. F.: Global satellite analysis of the relation between aerosols and short-lived trace gases, Atmos. Chem. Phys., 11, 1255–1267, doi:10.5194/acp-11-1255-2011, 2011.

Verhoelst, T., Compernolle, S., Pinardi, G., Lambert, J.-C., Eskes, H. J., Eichmann, K.-U., Fjæraa, A. M., Granville, J., Niemeijer, S., Cede, A., Tiefengraber, M., Hendrick, F., Pazmiño, A., Bais, A., Bazureau, A., Boersma, K. F., Bognar, K., Dehn, A., Donner, S., Elokhov, A., Gebetsberger, M., Goutail, F., Grutter de la Mora, M., Gruzdev, A., Gratsea, M., Hansen, G. H., Irie, H., Jepsen, N., Kanaya, Y., Karagkiozidis, D., Kivi, R., Kreher, K., Levelt, P. F., Liu, C., Müller, M., Navarro Comas, M., Piters, A. J. M., Pommereau, J.-P., Portafaix, T., Prados-Roman, C., Puentedura, O., Querel, R., Remmers, J., Richter, A., Rimmer, J., Rivera Cárdenas, C., Saavedra de Miguel, L., Sinyakov, V. P., Stremme, W., Strong, K., Van Roozendael, M., Veefkind, J. P., Wagner, T., Wittrock, F., Yela González, M., and Zehner, C.: Ground-based validation of the Copernicus Sentinel-5P TROPOMI NO$_2$ measurements with the NDACC ZSL-DOAS, MAX-DOAS and Pandonia global networks, Atmos. Meas. Tech., 14, 481–510, https://doi.org/10.5194/amt-14-481-2021, 2021.

Vigouroux, C., Hendrick, F., Stavrakou, T., Dils, B., De Smedt, I., Hermans, C., Merlaud, A., Scolas, F., Senten, C., Vanhaelewyn, G., Fally, S., Carleer, M., Metzger, J.-M., Müller, J.-F., Van Roozendael, M., and De Mazière, M.: Ground-based FTIR and MAX-DOAS observations of formaldehyde at Réunion Island and comparisons with satellite and model data, Atmos. Chem. Phys., 9, 9523–9544, https://doi.org/10.5194/acp-9-9523-2009, 2009.

Wagner, T., Deutschmann, T., and Platt, U.: Determination of aerosol properties from MAX-DOAS observations of the Ring effect, Atmos. Meas. Tech., 2, 495–512, https://doi.org/10.5194/amt-2-495-2009, 2009.

Wagner, T., Beirle, S., Brauers, T., Deutschmann, T., Frieß, U., Hak, C., Halla, J. D., Heue, K. P., Junkermann, W., Li, X., Platt, U., and Pundt-Gruber, I.: Inversion of tropospheric profiles of aerosol extinction and HCHO and NO2 mixing ratios from MAX-DOAS observations in Milano during the summer of 2003 and comparison with independent data sets, Atmos. Meas. Tech., 4, 2685–2715, https://doi.org/10.5194/amt-4-2685-2011, 2011.

Wagner, T., Beirle, S., Benavent, N., Bösch, T., Chan, K. L., Donner, S., Dörner, S., Fayt, C., Frieß, U., García-Nieto, D., Gielen, C., González-Bartolome, D., Gomez, L., Hendrick, F., Henzing, B., Jin, J. L., Lampel, J., Ma, J., Mies, K., Navarro, M., Peters, E., Pinardi, G., Puentedura, O., Puķīte, J., Remmers, J., Richter, A., Saiz-Lopez, A., Shaiganfar, R., Sihler, H., Van Roozendael, M., Wang, Y., and Yela, M.: Is a scaling factor required to obtain closure between measured and modelled atmospheric O$_4$ absorptions? An assessment of uncertainties of measurements and radiative transfer simulations for 2 selected days during the MAD-CAT campaign, Atmos. Meas. Tech., 12, 2745–2817, https://doi.org/10.5194/amt-12-2745-2019, 2019.

Wang, Y., Li, A., Xie, P. H., Wagner, T., Chen, H., Liu, W. Q., and Liu, J. G.: A rapid method to derive horizontal distributions

of trace gases and aerosols near the surface using multi-axis differential optical absorption spectroscopy, Atmos. Meas. Tech., 7, 1663–1680, https://doi.org/10.5194/amt-7-1663-2014, 2014.

1195 Wang, Y., Pukite, J., Wagner, T., Donner, S., Beirle, S., Hilboll, A., Vrekoussis, M., Richter, A., Apituley, A., Piters, A., Allaart, M., Eskes, H., Frumau, A., Roozendael, M. V., Lampel, J., Platt, U., Schmitt, S., Swart, D., and Vonk, J.: Vertical Profiles of Tropospheric Ozone From MAX-DOAS Measurements During the CINDI-2 Campaign: Part 1 – Development of a New Retrieval Algorithm, J. Geophys. Res.-Atmos., 123, 10637–10670, https://doi.org/10.1029/2018JD028647, 2018.

1200 Williams, J.E., Boersma, K.F., LeSager,P., and Verstraeten, W.W.: The high-resolution version of TM5-MP for optimized satellite retrievals: description and validation, Geosci. Model Dev., 10, 721–750, https://doi.org/10.5194/gmd-10-721-2017, 2017.

Wittrock, F., Oetjen, H., Richter, A., Fietkau, S., Medeke, T., Rozanov, A., and Burrows, J. P.: MAX-DOAS measurements of atmospheric trace gases in Ny-Ålesund - Radiative transfer studies and their application, Atmos. Chem. Phys., 4, 955–
1205 966, https://doi.org/10.5194/acp-4-955-2004, 2004.

1210

1215

1220